MULTIPHOTON IONIZATION OF MOLECULES EMBEDDED IN SUPERFLUID LIQUID HELIUM DROPLETS

by

Elena Polyakova

A Dissertation Presented to the
FACULTY OF THE GRADUATE SCHOOL
UNIVERSITY OF SOUTHERN CALIFORNIA
In Partial Fulfillment of the
Requirements for the Degree
DOCTOR OF PHILOSOPHY
CHEMISTRY (CHEMICAL PHYSICS)

August 2005

Copyright 2005 Elena Polyakova

Acknowledgements

First, I would like to express my sincere appreciation to my scientific advisor, Curt Wittig, for introducing me to the exciting world of helium droplets. Second, I wish to acknowledge Ilya Bezel and Daniil Stolyarov who welcomed me into the laboratory and taught me almost everything I know.

I am very grateful to Professors Hanna Reisler, Stephen Bradforth, Anna Krylov, and Andrei Vilesov for hard questions and useful discussions, as well as for giving me valuable advice. I wish to thank all members of Prof. Janda's group (Department of Chemistry, University of Irvine, California) as well as Klaas Nauta and Kun Lu for help in design of the helium machine. Additionally, I would like to acknowledge the personnel of the USC Machine Shop, Victor Jordan and colleagues, for providing a tremendous amount of assistance in building the helium droplet machine.

Thanks must go to all members of the Department staff: Michele Dea, Heather Meunier, Yuki Yabuta, Jennifer Torres, Mary Pacheco, Ross Lewis, and Frank Niertit. Because of their endless efforts, the only problems we had to deal with were the scientific ones. Special thanks are also in order to all my fellow graduate students and postdocs in SSC for friendship, debates, use of laboratory equipment, and continuous support. I always feel like I have a big family here at USC.

Finally, I want to wish the best of luck and a lot of new results to Anton Zadorozhnyy and Christopher Nemirow who recently joined the helium droplet project.

Table of Contents

Acknowledgements ii

List of Figures vi

List of Tables xi

Abstract xii

Chapter 1: Introduction 1

Chapter 2: Concepts 4
- 2.1. Helium droplet beams 4
  - 2.1.1. Production of helium droplet beams 4
  - 2.1.2. Properties of helium droplet beams 7
  - 2.1.3. Capture of foreign species 10
- 2.2. Interaction of helium with impurities 14
  - 2.2.1. Electrons in liquid helium 15
  - 2.2.2. Electrons in high density helium gas 19
  - 2.2.3. Escape of electron from helium cluster 21
- 2.3. Interaction of helium with positive impurities 25
- 2.4. Location of species in helium droplets 27
- 2.5. Ionization in helium droplet 28
- 2.6. References 37

Chapter 3: Experimental Apparatus 42
- 3.1. Vacuum system 42
- 3.2. Cryogenic nozzle design 48
- 3.3. Cryogenic droplet source 50
- 3.4. Laser system and optics 52
- 3.5. Time of flight mass spectrometry and data analysis 56
- 3.6. References 59

Chapter 4: NO molecule 60
- 4.1. Spectroscopy of NO molecule 60
- 4.2. NO trapped in matrices 65

4.3. NO – rare gas complexes 71
4.4. References 73

Chapter 5: Results 76
5.1. Multiphoton ionization of NO by nanosecond pulses 76
5.1.1. TOF spectrum 76
5.1.2. Wavelength dependence of TOF spectra 78
5.2. Discussion of ionization mechanism 82
5.2.1. General mechanism of multiphoton ionization 82
5.2.2. Surface bound NO* Rydberg bubble 85
5.2.3. Liberation of $(NO \cdot He_m)^+$ clusters 87
5.2.4. Vibrational relaxation of NO^* 90
5.3. Discussion of wavelength dependence 91

5.4. Future experimental work 95
5.5. References 101

Bibliography 103

Appendixes 107
Appendix A. Alignment of a helium droplet machine with a telescope 107
Appendix B. Nozzle check-up procedure 110
Appendix C. The procedure of the nozzle alignment 112
Appendix D. The laser beam alignment 113

List of Figures

Figure 2-1. The pressure-temperature phase diagram of He. **6**

Figure 2-2. Overview of the mean numbers and liquid-droplet diameters (Å) of He droplets formed in different types of continuous modes of jet operation..... **8**

Figure 2-3. Helium cluster size distribution at several nozzle temperatures obtained in scattering experiments at He stagnation pressure 80 bar. Least-squares fits to log-normal distribution are shown in solid lines..... **9**

Figure 2-4. Droplet beam speeds in the subcritical expansion regime (P = 20 bar)..... **11**

Figure 2-5. Dependence of the depletion signal on SF_6 pressure in the pick-up cell, as measured for the absorption bands for $(SF_6)_k$ complexes with different k values..... **12**

Figure 2-6. Cooling of droplets with $\overline{N} \sim 3000$ due to evaporation from the surface..... **14**

Figure 2-7. Density profiles for an electron bubble in bulk liquid helium. Solid line: helium density. Dashed line: electron density. **16**

Figure 2-8. Equilibrium electron bubble radius versus pressure **16**

Figure 2-9. Bubble dynamics in liquid helium. The time dependence of the increase of the radius R for the expansion of the bubble (solid circles). The collapse of the empty bubble (open circles). **18**

Figure 2-10. The dependence of mobility of electrons in dense helium gas upon gas density **20**

Figure 2-11. Drift velocity of an electron in dense helium gas versus field strength for T = 4.19K. **21**

Figure 2-12. Bubble potential energy curve near the surface of liquid helium **22**

Figure 2-13. Sketch of external and internal states of an electron in a droplet. **23**

Figure 2-14. Bubble life time in helium clusters as a function of droplet size **24**

Figure 2-15. Helium density profiles for the Na^+-He_N clusters at T= 1.0 K. The origin is set to be the position of Na^+. The number of helium atoms is 30, 40, 60, and 100 starting from the curve with the lowest amplitide. The bulk liquid density is indicated by dashed line. **26**

Figure 2-16. Schematic diagram of the mechanism of electron bombardment ionization..... **30**

Figure 2-17 Mass spectrum of pure helium clusters with <N> = 15000..... **31**

Figure 2-18 Mechanism of laser induced ionization..... **34**

Figure 2-19. Photoelectron energy distribution for a photon energy of 23.8 eV..... **35**

Figure 3-1. A – Photograph of the helium droplet machine, B-Schematic diagram of the experimental apparatus, I. Helium droplet source chamber, II. pickup chamber, III. detection chamber, IV. quadrupole mass-spectrometer chamber. 1a,b –closed cycle refrigerators, 2 – nozzle, 3 – pickup cell 4 – cold finger, 5 – copper plate, 6 – set of electrodes, 7 – MCP (microchannel plate),8 – quadrupole mass-spectrometer, 9 – diffusion pump, 10 a,b,c – turbo-molecular pumps. **43**

Figure 3-2. Plot of the relative intensities of monomers, dimers and pure droplets **44**

Figure 3-3 Cryogenic nozzle arrangement: 1- brass nut, 2 – aperture, copper disk with 5μm aperture 3 – indium gasket, 4 – copper nozzle, 5 – teflon washer, 6-stainless steel holder **49**

Figure 3-4. Nozzle tip:1 – copper nozzle, 2 – indium gasket, 3 – copper aperture, 4 – brass nut **49**

Figure 3-5. XY- motion translational stage. A silicon diode is connected to the surface a of the nozzle, a copper braid – surface b, and helium gas inlet – surface c. **51**

Figure 3-6. Silicon diode sensor assembly **52**

Figure 3-7. Ion detection arrangemen (not to scale): (a) set of electrodes; (b) TOF region; (c) MCP; 1- repeller electrode, 2 – extractor electrode, 3 – grounded shield **56**

Figure 3-8. Time of flight spectrum of NO embedded in helium droplet. A – full range *m/Z=0-100* amu, B– the same mass range as in Fig. A but with $\times 10$ vertical scale, C – mass range *m/Z=32-40* amu. **58**

Figure 4-1. Schematic diagram of potential curves of NO. **61**

Figure 4-2. Radius of Rydberg orbital (in Ångstroms) as a function of the principle number of this orbital. **63**

Figure 4-3. Schematic illustration of the mechanism of absorption and emission in the bubble Rydberg model. **65**

Figure 4-4. Excitation spectrum of global fluorescence of NO in solid krypton. **66**

Figure 4-5. Fluorescence signal of the NO $A^2\Sigma$ (0, υ″) emission as a function of probe wavelength. The dips represent depletion of the fluorescence signal due to depopulation of the $A^2\Sigma$ state to higher Rydberg states **71**

Figure 5–1. Example of TOF mass spectrum of ions formed as the result of multiphoton ionization of NO embedded in helium droplets ($h\nu$ = 24330 cm^{-1}). The most intense peak corresponds to the NO^+ ion (m/Z = 30 amu.). A progression of $(NO{\cdot}He_m)^+$ clusters (m/Z = 34, 38, 42, 46… amu.) is shown at the insert, the signal from $(NO{\cdot}He_m)^+$ fragments is magnified 10 times. Top axis shows the amount of helium atoms attached to NO core.
77

Figure 5–2. Mass selected MPI spectrum of NO molecule in helium droplets. The intensities of the signal from $(NO{\cdot}He_m)^+$ ions at m/Z= 30+4·n amu, n = 0…9 were integrated for all TOF spectra in the range 23250 – 27816 cm^{-1} **79**

Figure 5–3. Mass selected MPI spectrum of the NO molecule in helium droplets. Formation of (NO·He)+ was monitored. A –Signal at mass 34 integrated for TOF traces recorded for every 60 cm-1 in the region 22,222-27,816 cm-1. B – The ion signal at amu 34 recorded directly in the region 24,185-24,445 cm-1 with resolution 1 cm-1 and 10000 averaging. (solid line) The spectrum low-resolution spectrum, which is shown in Fig. A in the same region (doted line). **80**

Figure 5-4. Ionization scheme of the NO molecule in gas phase. **83**

Figure 5-5. Scheme of multiphoton ionization of the NO molecule in helium droplets. Step 1 – Vertical

electronic excitation of the NO molecule from the ground state to the low Rydberg state. Step 2 – Motion of the Rydberg bubble toward the surface of the helium cluster. Step 3 – immediate ionization and formation of $(NO{\cdot}He_m)^+$ clusters. **84**

Figure 5–6. Schematic diagram of the mechanism of snowball liberation **88**

Figure 5-7. Two-photon ionization scheme. **96**

Figure 5–8 Example of TOF mass spectrum of ions formed as the result of two-photon ionization of the NO molecule embedded in helium droplets ($h\nu$ = 47000 cm^{-1}) **97**

Figure 5-9. Example of TOF mass spectrum of ions formed as the result of multiphoton ionization of NO clusters embedded in a helium droplet ($h\nu$ = 28169 cm^{-1}, τ = 30 ps, E=100 mJ/pulse) There are 2.5 NO molecules pre droplet in average.

Figure 5-10. Schematic diagram of photoexcitation of NO_2 in helium droplets above the gas phase dissociation threshold **100**

Figure 5-11. Schematic drawing of laser arrangement for proposed picosecond pump-probe experiment..... **100**

List of Tables

Table 3-1. Output of UVT system. **54**

Table 4-1. Parameters of low electronic states of NO (from references 1 and 8) **63**

Table 4-2. Gas-matrix absorption shifts and linewidth of the lowest Rydberg state $A^2\Sigma$ ($\upsilon = 0$)..... **68**

Abstract

In the experiments presented in this Dissertation, the helium droplet isolation technique that has recently proven to be a powerful tool in the hands of physical chemists is combined with multiphoton ionization (MPI) laser spectroscopy to address the dynamics of the interaction of an impurity with a superfluid helium host.

First, the MPI of NO molecules trapped inside of helium droplets is investigated in the near UV. Time-of-flight spectra demonstrate the formation of $(NO{\cdot}He_N)^+$ clusters with N = 0…40. Three or four photons are required for ionization in this range. The multiphoton ionization is believed to be a multistep process. At first, the NO molecule is excited into its low-lying Rydberg state. The overlap of the electron densities of the helium atoms and the Rydberg electron results in a blue shift and broadening.

Helium is repelled by the Rydberg electron and moves away, and bubble-like NO^* is created. NO^* will move toward the surface of the helium droplet. The surface energy accumulated in the free surface of the molecular-helium interface is released and dissipated by the droplet, and the molecule stays attached to the helium droplet in a dimple. The fact that NO* resides at the surface facilitates its photoionization. This transport process occurs concomitantly with vibrational relaxation of the NO* moiety in the event that the NO^+ is formed with vibrational

excitation. The next step is ionization. NO* absorbs one or two photons close to the surface of the droplet. The subsequent ejection of an electron from NO* into vacuum creates an NO^+ moiety at the edge of the droplet. Helium is attracted strongly to this ion, ensuring vigorous dynamics in which a helium snowball is formed around the NO^+ as concomitant evaporation cools and stabilizes the snowball, yielding small positive ions of the form $(NO{\cdot}He_m)^+$.

Chapter 1: Introduction

The material in this Dissertation is ordered as follows. This chapter presents the outline of the dissertation. Chapter 2 gives a detailed description of the helium droplet isolation technique, evaporative cooling, and quantitative properties of helium beams. Section 2.1 outlines historical aspects, as well as fundamental properties and methods of production of the helium droplet beams. Sections 2.2-2.4 focus on specifics of the interaction of helium with different types of impurities. Specifically, the model that helps to predict if the impurity is localized near the surface or at the center of the droplet is presented. Section 2.5 provides a brief survey of the process of ionization of species in /on helium droplets. As no complete theory of ionization in helium droplets has been developed yet, several hypotheses of ionization mechanisms are discussed, and a summary of the most recent experimental investigations is presented.

As a part of this work, a new helium droplet machine has been designed, built and made operational. A detailed description of this helium droplet machine, including the cryogenic helium source, the home-built TOF mass spectrometer, and the pick-up cell are provided in Section 3. Section 3.4. is dedicated to the laser system and optical arrangements used to generate visible and UV radiation.

Chapter 4 is devoted to spectroscopy of the NO molecule. Section 4.1 summarizes the available theoretical and experimental data on properties of Rydberg states of free NO. The fate of Rydberg states is considered for NO molecules confined in rare-gas matrices (Section 4.2.) and for van der Waals NO·Rg (Rg- rare gas) complexes (Section 4.3.).

In Chapter 5, the most important results on multiphoton ionization of NO molecule embedded in helium droplets are summarized. In the experiment described in Section 5.1, the formation of ions was observed upon excitation of helium droplets doped by NO molecules by laser radiation in the range 22,222 – 27,816 cm^{-1} , which corresponds to the excitation of low lying vibrational states of the $A^2\Sigma$ electronic state.

In Section 5.3., a great deal of attention is paid to the discussion of mechanism of ionization, as it was found to be a complicated multistep process. All of the above is discussed in Section 5.4 within the context of a model that includes the relevant phenomena such as accidental resonances with high Rydberg states, efficient vibrational relaxation of the NO moiety, and motion of electronically excited NO^* toward the surface of the helium cluster, which accounts many of the observations.

Section 5.5 presents our preliminary results as well as several possible future experiments. It was found that in the case of picosecond ionization, the formation of large $(NO{\cdot}He_N)^+$ clusters is more efficient than it is for ionization in the nanosecond regime. Ionization of NO in the picosecond regime opens the

possibility of studying the dynamics of excited NO as it moves through the droplet.

The appendices cover the alignment procedures and check-up procedures required for assembly or modification of the helium droplet machine.

Chapter 2: Concepts

2.1. Helium droplet beams

2.1.1. Production of helium droplet beams

The first experimental evidence of the formation of helium droplets dates back to 1908 and is attributed to H. Kamerlingh Onnes. During one of his initial attempts to liquefy helium, he observed a "dense gray cloud [...] resembling partly cotton wool" in an expansion of cold, gaseous helium. [1] In 1961 Becker and coworkers demonstrated that helium droplets can be produced by supersonic expansion of high purity helium gas though a cooled nozzle into a vacuum chamber. [2] After this seminal work, helium droplet beams received a great deal of attention. In the 1970's, mass-spectrometric studies of pure clusters addressed the enhanced ion stability of small helium clusters, i.e. "magic numbers". [3] An important breakthrough was made in 1990, when the Toennies group in Gottingen reported the first definitive evidence that helium clusters readily capture foreign particles. (see Section 2.1.3.) By varying the temperature and pressure of the nozzle, one can achieve three qualitatively different regimes of expansion (isentropic conditions are assumed): [4]

- Subcritical: Small droplets with $\overline{N} < 5 \times 10^4$ are formed. This regime was maintained during all experiments described in the present dissertation.
- Critical: The expansion isentrope passes directly through the critical point of helium ($T_c(^4He)$=5.2*K*, $P_c(^4He)$=2.27 *bar*) [3]
- Supercritical: T<10K. This regime is characterized by bimodal droplet size distribution. Major portion of the beam are the large helium droplets with mean cluster size $\overline{N} > 10^6$. In addition, smaller droplets with $\overline{N} = 10^4$-10^5 are formed from gas atoms evaporated from large droplets.

Figure 2-1 shows the pressure-temperature phase diagram of helium, and dashed lines represent typical subcritical (lower curve) and supercritical (upper curve) expansion isentropes.

Along the line of the helium expansion, density and temperature of the expanding gas drop rapidly as the distance from the nozzle increases. The characteristics of helium droplets beams formed in the normal continuous expansion have been investigated in detail, and for the nozzle aperture d_0=5 μm, stagnation temperatures T_0= 6-25 K, and helium source pressures p_0 = 5–100 bar, such parameters as mean cluster size $\overline{N}$, cluster size distribution and helium beam velocity are discussed in the next section.

The intensity of the beam in the subcritical regime has been measured to be 10^{20}-10^{21} atoms/sterad·s. [5] The clusterization degree in this regime is below 10%. Therefore, most of the gas flow must be evacuated by a pumping system. The pressure in the vacuum chamber must be kept below 10^{-3} Torr to prevent beam attenuation.

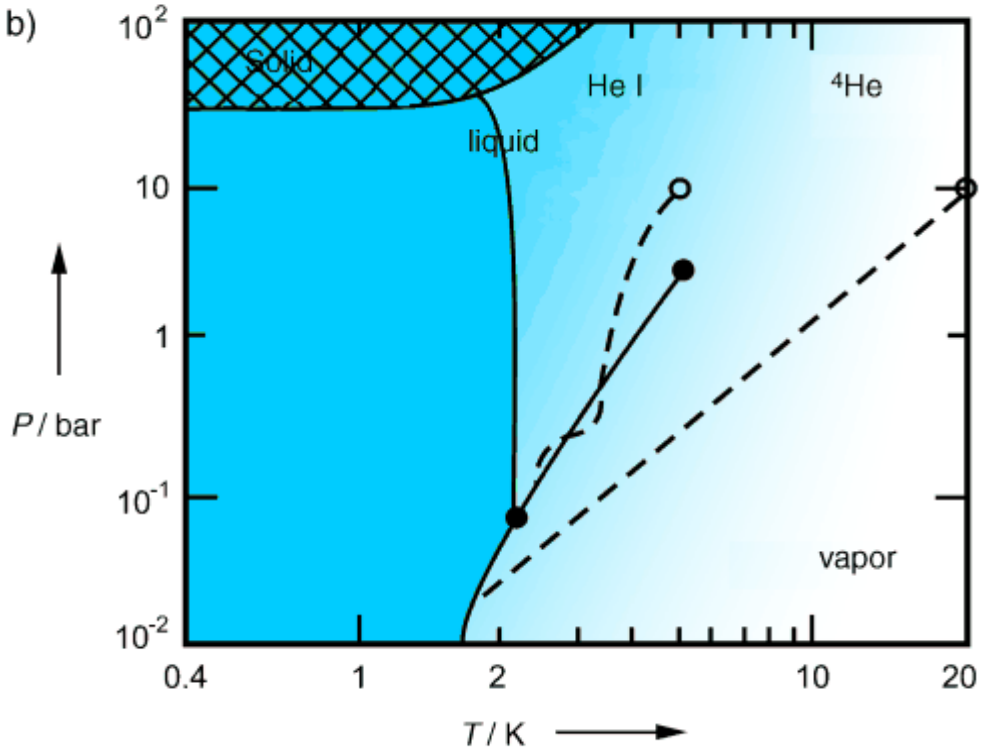

Figure 2-1. The pressure-temperature phase diagram of He.

For that reason, the main physical limitation of the beam intensity is the pumping speed of the vacuum system. The maximum number density of the droplets obtainable for experimental studies is only 10^9 - 3×10^{10} cm^{-3}, which is below the limit of sensitivity of many common spectroscopic techniques such as

direct absorption or scattering. Thus, achievement of a feasible signal to noise ratio is a lasting experimental challenge.

Recently, a pulsed droplet nozzle (30-50 μs) has been used with successfully in the Vilesov group. [6] The peak density of droplets is higher by at least two orders of magnitude than it is for a continuous beam. The superior signal to noise ratio (S/N) was demonstrated for LIF of embedded organic molecules. Unfortunately, the possibility of the formation of clusters with less than 10^4 helium atoms has not been achieved yet. For this reason, experimental applications of the pulsed beam are limited.

Recently, Toennies and coworkers introduced a method to produce micron-sized helium droplets. [7] Clusters with $\overline{N}$ =10^{10}-10^{12} have been produced in the expansion of superfluid helium under pressure into a vacuum chamber. (Fig. 2-2, top curve)

2.1.2. Properties of helium droplet beams

Assuming a helium droplet of spherical shape and bulk density of helium, the diameter D_D of a helium droplet composed of N atoms can be estimated from formula (2.1)

$$D_D = 2r_0 N^{1/3} \qquad (2.1)$$

where r_0 equals 2.22 Å.

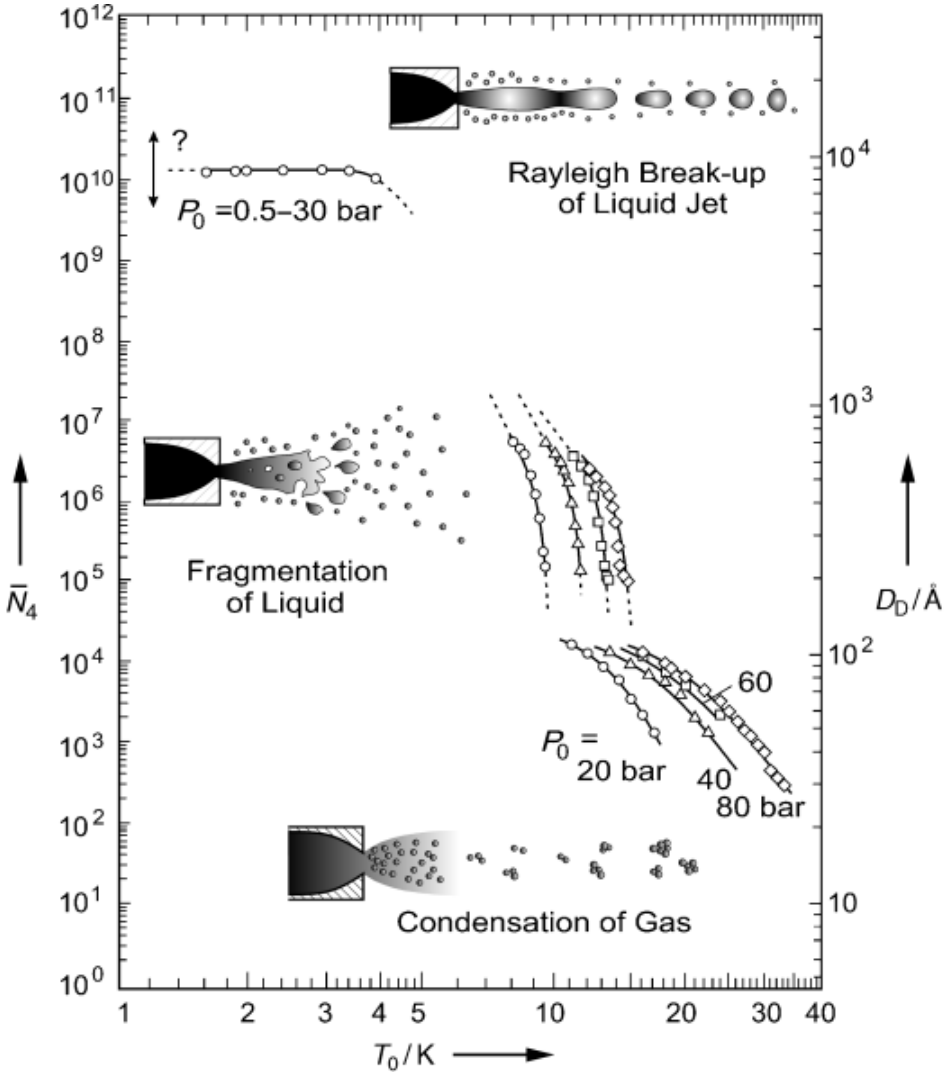

Figure 2-2. Overview of the mean numbers and liquid-droplet diameters (Å) of He droplets formed in different types of continuous modes of jet operation.

Figure 2-2 provides an overview of the mean number sizes $\overline{N}$ and liquid-droplet diameters (D_D) of helium droplets for different stagnation temperatures and types of continuous expansion. [8] Referring to Fig. 2-2, the four curves in the middle region correspond to different source pressures: 20 (○), 40 (Δ), 60 (□) and 80 bar (◊). The smallest clusters are obtained in subcritical expansions. These data were obtained by deflecting the droplets through the impact of atoms from a secondary beam. Parameters for large droplets ($\overline{N} > 10^5$) were obtained by means of deflection of the negatively charged droplets by electric field. [5]

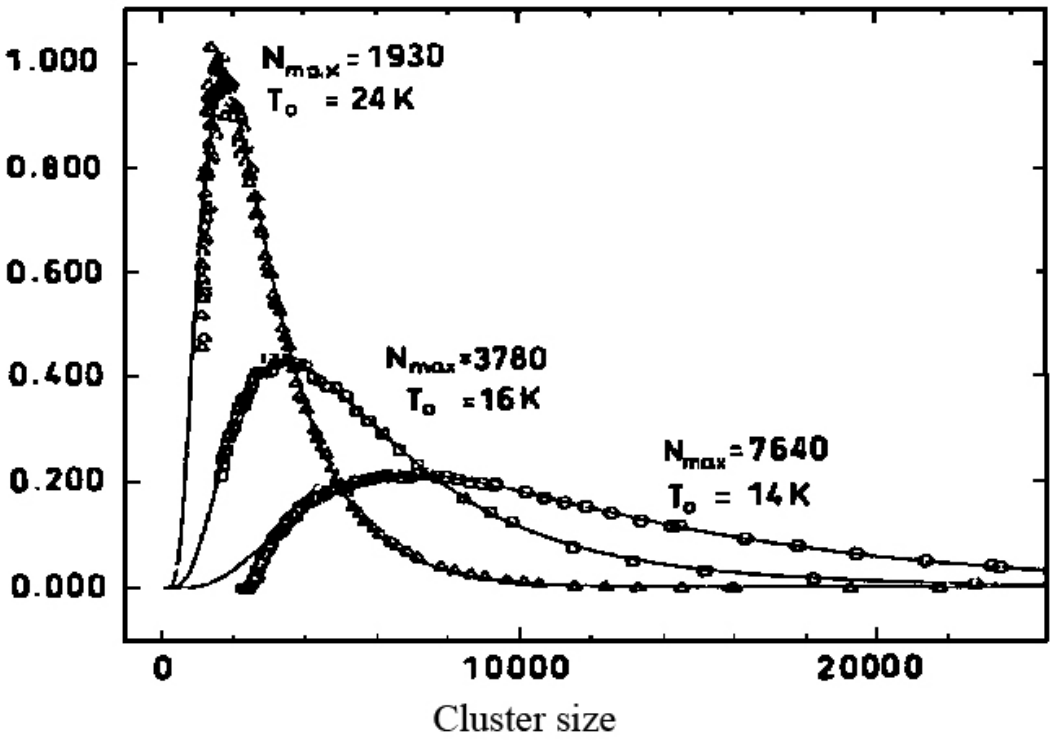

Figure 2-3. Helium cluster size distribution at several nozzle temperatures obtained in scattering experiments at He stagnation pressure 80 bar. Least-squares fits to log-normal distribution are shown in solid lines

Another important parameter of the cluster beam is the width of size distribution. Scattering measurements have shown that the size distribution follows a log-normal form:

$$P_N(N) = \frac{1}{2\pi N\sigma}\exp\left(-\frac{(\ln N - \mu)^2}{2\sigma^2}\right) \qquad (2.2)$$

Size distributions for clusters formed at stagnation pressure of 80 bar for a range of temperatures from 14 - 24 K obtained in the scattering experiments [9] are shown in Fig. 2-3. It is noteworthy that this distribution is extremely broad for the large droplets and may contribute to the broadening of spectral lines. Another characteristic of the cluster beam, which changes with source conditions, is the beam velocity and $\frac{\Delta v}{v}$ distribution. The mean velocity of the helium droplet beam ranges from 250 m/s to 450 m/s (Figure 2-4). The velocity distribution is extremely sharp: $\frac{\Delta v}{v} \approx 0.01 - 0.03$. [4]

2.1.3. Capture of foreign species

The number of systems subjected to detailed analysis in liquid helium is modest. Achieving the concentration of single molecules suitable for spectroscopic studies is a well known experimental challenge. To date, the only species studied in detail in helium are metal atoms and ions as well as intrinsic impurities.

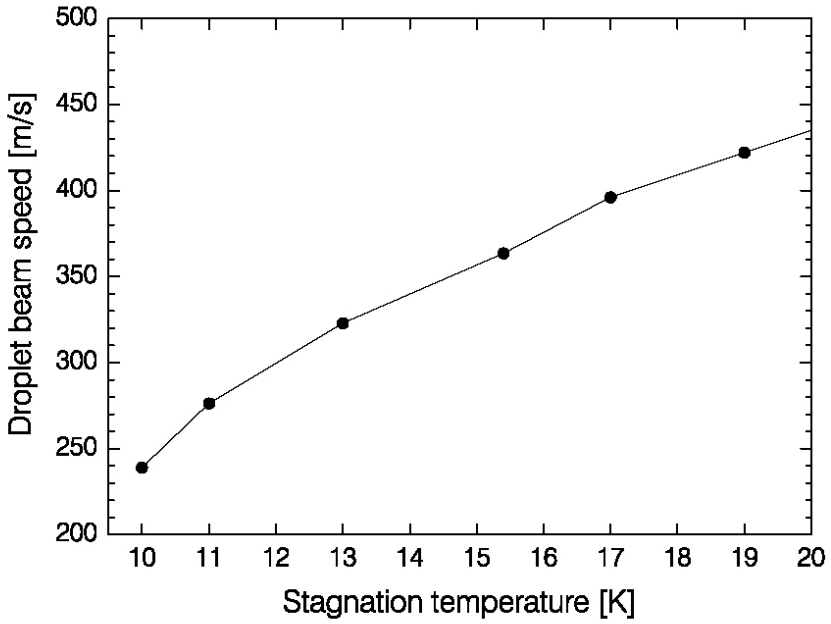

Figure 2-4. Droplet beam speeds in the subcritical expansion regime (P = 20 bar).

The internal pressure of helium droplets is ~ 2 bar [8], which is significantly lower than the pressure required for solidification (25 bar), as can be seen in Fig. 2-1. Therefore, helium is a substance which is capable of forming liquid clusters. Doped helium droplets can be formed by passing the pure clusters through a low-pressure gas. In 1985, a similar effect was demonstrated by Scoles and coworkers for solid argon clusters. [10]

Toennies and coworkers not only confirmed that both atomic and molecular guest species can be introduced effortlessly this way, but also that the aggregation of impurities to subclusters inside the droplets can be controlled in a quantitative manner. [3] The probability for pick-up of k particles is given by a Poisson distribution (Formula 2.3),

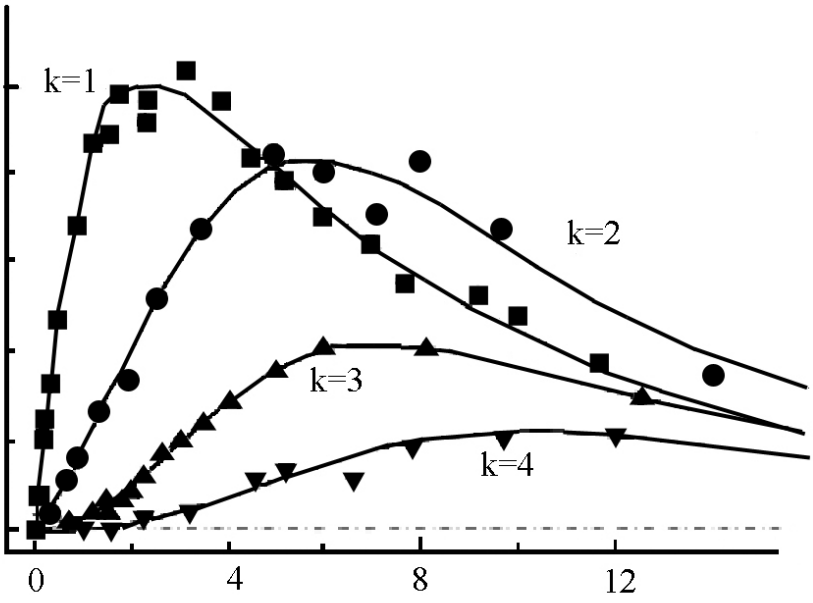

Figure 2-5. Dependence of the depletion signal on SF_6 pressure in the pick-up cell, as measured for the absorption bands for $(SF_6)_k$ complexes with different k values.

$$P_k(z) = (z)^k \exp(-z)/k! \qquad (2.3)$$

where z is the average number of collisions which lead to capture of the particles by the droplet. [3]

To illustrate this statement, the dependence of the depletion signal on the SF_6 pressure in the pick-up cell is given in Fig. 2-5. The parameter z can be estimated from the collision cross section, the length of the pickup region, and the gas pressure in this region. It was found that the cross section of inelastic collision is close to the geometric cross section of the helium droplet, which can be easily estimated from Fig. 2-2. The pressure of gas required to pickup one molecule per cluster is ~10^5 Torr.

Several pickup techniques can be used to introduce guest molecules, atoms and radicals into a vacuum scattering cell: gases are delivered though pressure reducers; substances with low volatility are heated in an oven inside the vacuum chamber, radicals [11] , atoms and clusters of metals with low vapor pressure are produced by pyrolysis and laser ablation [12], respectively, *in situ*.

2.1.4. Evaporative cooling

Formed by condensation of helium close to the cryogenic nozzle, in collision-free regime (The distance from the nozzle is larger than 1000 aperture diameters [4]), helium droplets undergo efficient cooling due to the evaporation from the droplet surface. Figure 2-6 shows illustrates of this process for droplets having $\overline{N} \sim 3000$. Starting at 1 K (solid line) and 0.7 K (dashed line), the internal temperature decreases rapidly. According to Stein, the initial rate is 10^{10} K/s [13]. After about 10^{-7} s, the droplet temperature does not depend upon initial condition. The droplets are predicted to attain temperatures of about 0.3 K within a typical experimental flight time of 1 ms. [14] A temperature of 0.37 K was estimated from rovibrational spectra of embedded molecules. [3] This mechanism must be taken into consideration for the pickup process. (Section 2.1.3) Following an inelastic collision between a foreign molecule and a helium droplet, the kinetic energy of the collision, the molecule's internal energy and the binding energy of the impurity to the droplet will be dissipated to the droplet. On average, the pickup of one molecule leads to evaporation of 300-600 helium atoms. [15]

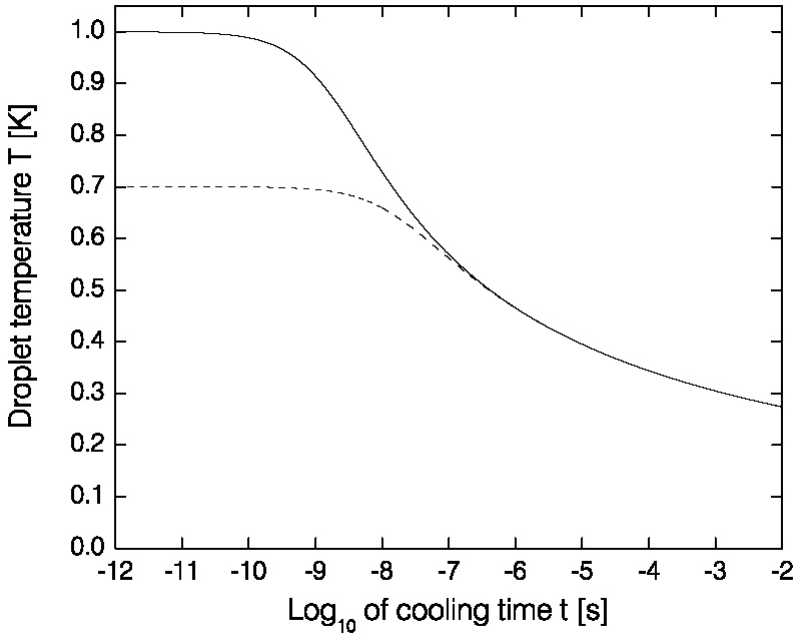

Figure 2-6. Cooling of droplets with $\overline{N}$ ~ 3000 due to evaporation from the surface. Solid line: initial temperarture is 1 K. Dashed line – 0.7K

Similarly, excitation of the internal molecular degrees of freedom by laser radiation is transferred to degrees of freedom of the helium. This energy is dissipated by evaporative cooling causing the shrinkage of the cluster. The reduction of geometrical cross section of helium droplets can be investigated by mass spectrometry, which will be discussed in the next section.

2.2. Interaction of helium with impurities

One of the weakest in nature, the interaction between helium and a embedded host is a fascinating issue. This interaction is weaker by several orders of magnitude than the interaction of a solute molecule with a solvent in a typical

solution. When charged species are embedded in helium, the strong interaction of the ion with helium leads to a dramatic rearrangement of helium near the ion. An intriguing fact is that the chemical potential can be changed if an atom or a molecule is promoted from the ground to the excited electron state. In the case of helium droplets, electron excitation can force the impurity to float on the surface of the droplet; or be ejected from the droplet. This chapter focuses on understanding the physical processes of helium-impurity interactions.

2.2.1. Electrons in liquid helium

The injection of a electron into helium requires more than 1eV of energy due to strong Pauli repulsion. [16] After the first experimental studies of electron bubbles in bulk liquid helium were carried out by Northby and Sanders in 1967 [17], it was known that electrons reside in a cavity of radius ≈ 17 Å at zero pressure. Figure 2-7 shows the density profiles of helium and an electron calculated by Ancilotto and Toigo. [18] The formation of the cavity can be easily understood with the help of a simple "bubble model". According to this model, the total energy of the electron bubble (E_T) can be written

$$E_T = E_e + \frac{4}{3}\pi R^3 P + 4\pi R^2 \sigma \qquad (2.4)$$

where the first term, $E_e = \hbar^2 \pi^2 / 2m_e R^2$, is the ground state electronic energy, the second term is PV, i.e. the work done to form the cavity inside the liquid, and the third term is the surface energy, σ = 0.341 erg/cm^2. At equilibrium, the following dependence exists between the radius of the bubble and the pressure:

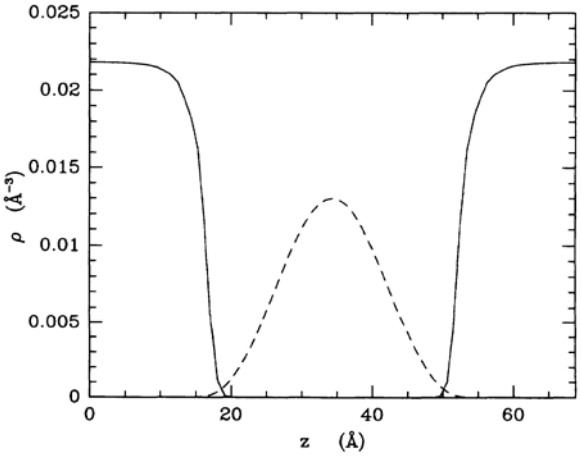

Figure 2-7. Density profiles for an electron bubble in bulk liquid helium. Solid line: helium density. Dashed line: electron density.

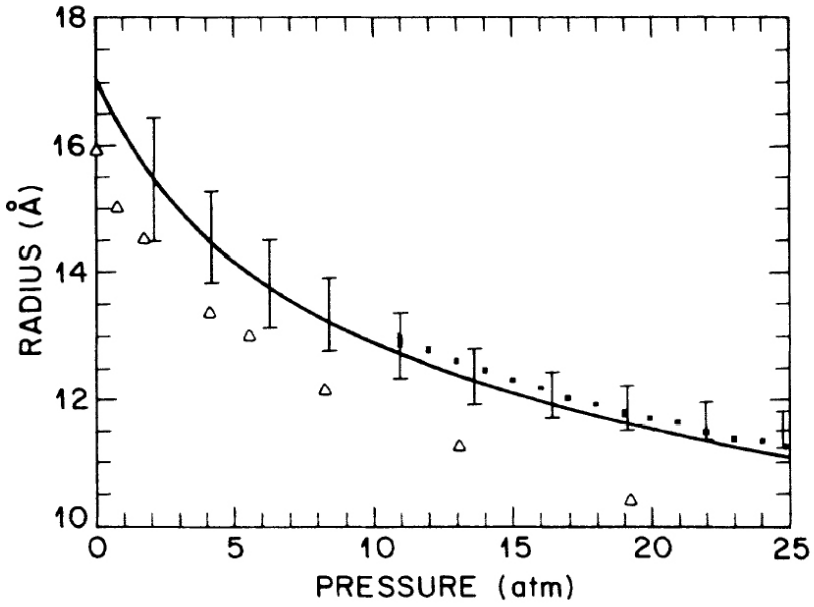

Figure 2-8. Equilibrium electron bubble radius versus pressure.

$$P = \frac{\hbar^2 \pi}{4 m_e R^5} - \frac{2\sigma}{R} \tag{2.5}$$

The validity of equation (2.4) has been checked by many experimental techniques as can be seen from Fig. 2-8. The solid line represents the radius calculated with the help of equation (2.4), and the thin bars are the radii that were measured by Ostermeier et al. in photon-limited mobility measurements.[19] The thick bars (some of them look like dots on Fig 2-8 due to small error bars) denote radii deduced by Ellis et al. from bubble acceleration measurements. [20] Finally, the open triangles result from Springett's experiments, in which the bubble trapping cross section on vortex lines was estimated. [21]

The mechanism and dynamics of bubble formation is of our special interest. According to Rosenblit and Jortner, this process can be described on the basis of the following assumptions [22]: The initial electron localization in the incipient bubble of radius $R_0 \approx 3.5$ Å is fast on the timescale of bubble formation. From dense gas electron localization experiments, the time of incipient bubble formation is estimated to be ~100 fs. The spherical shape of the bubble is being retained during the expansion; energy dissipation during the expansion can be neglected. Northby et al. [23] provided a rough estimate of the characteristic time for bubble formation:

$$\tau \sim R_{bubble} / \upsilon_s \qquad (2.6)$$

where υ_s =240 m/s is the speed of sound in helium.

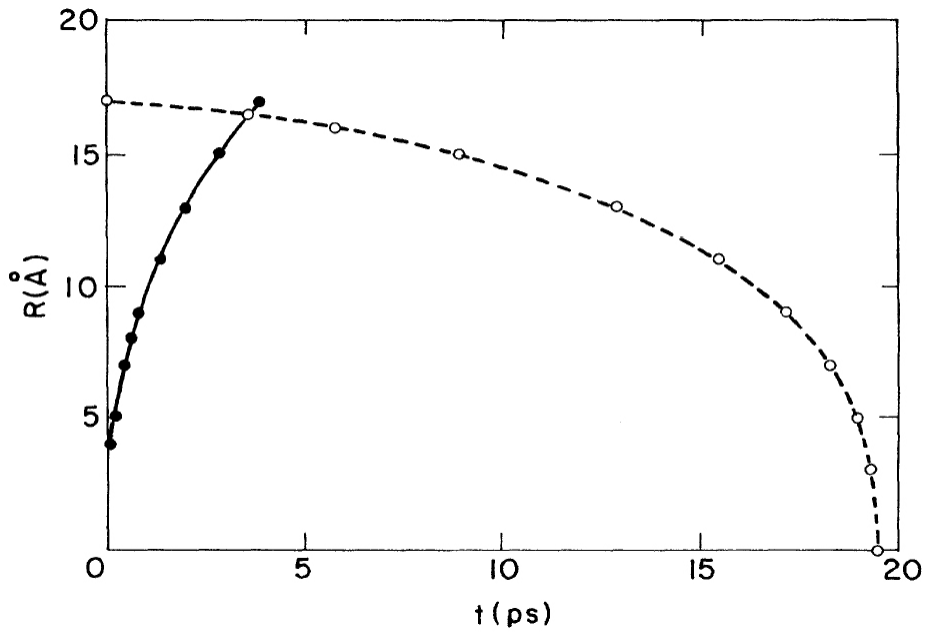

Figure 2-9. Bubble dynamics in liquid helium. The time dependence of the increase of the radius R for the expansion of the bubble (solid circles). The collapse of the empty bubble (open circles).

A bubble radius of 15 Å occurs on ~6 ps. The validity of this approach was verified by experiments by Hernandez and Silver ($\tau \sim 2$ ps) [22] and theoretical work by Rosenblit and Jortner ($\tau \sim 3.9$ ps) [22]. The latter provides a dynamic picture of bubble formation (Fig. 2-9, solid circles) and bubble collapse (Fig. 2-9, open circles). The time scale of bubble collapse is 20 ps, which can be used for an estimation of the "snowball" formation time. Mobility of the bubble in liquid helium was measured by R. M. Ostermeier in 1973. [19] For T = 0.415 K and P = 2.11 bar, the mobility was found to be 480 $cm^2 V^{-1} sec^{-1}$. If the motion of

an electron through the droplet is similar to the motion of an electron bubble in liquid helium, an electron would move with the speed 10 Å/ps.

2.2.2. Electrons in high density helium gas

Formed as the result of photoionization inside the helium droplet, an electron must travel through a layer of helium to escape from the droplet. The temperature of the helium droplet can be higher than 0.37 K if evaporative cooling has had insufficient time to cool the droplet following deactivation of dopant excitation. In this case the motion of an electron through dense helium gas could be a good model for the motion of an electron through the droplet.

Summarizing the results of numerous theoretical and experimental works [24], at the low pressure and high temperature of dense helium gas, electrons are not localized and have large mobility. The scattering of an electron on helium atoms is elastic and well described by binary collisions with known cross sections.

The mobility of an electron can be reliably predicted by classical kinetic theory. At higher gas densities and lower temperatures, the mobility of an electron drops by several orders of magnitude [24] as can be seen from Fig. 2-10. [25]

In this case, an electron is believed to form a spatially localized state inside a dilation of the fluid. The nature of this state is not yet understood. The electron can form a bubble, as in the case of liquid helium described above. On the other hand, the electron can be localized in the Anderson sense. In the latter

case, the wave function of the electron decays exponentially with the distance due to multiple scattering induced by the disorder of the medium. [26]

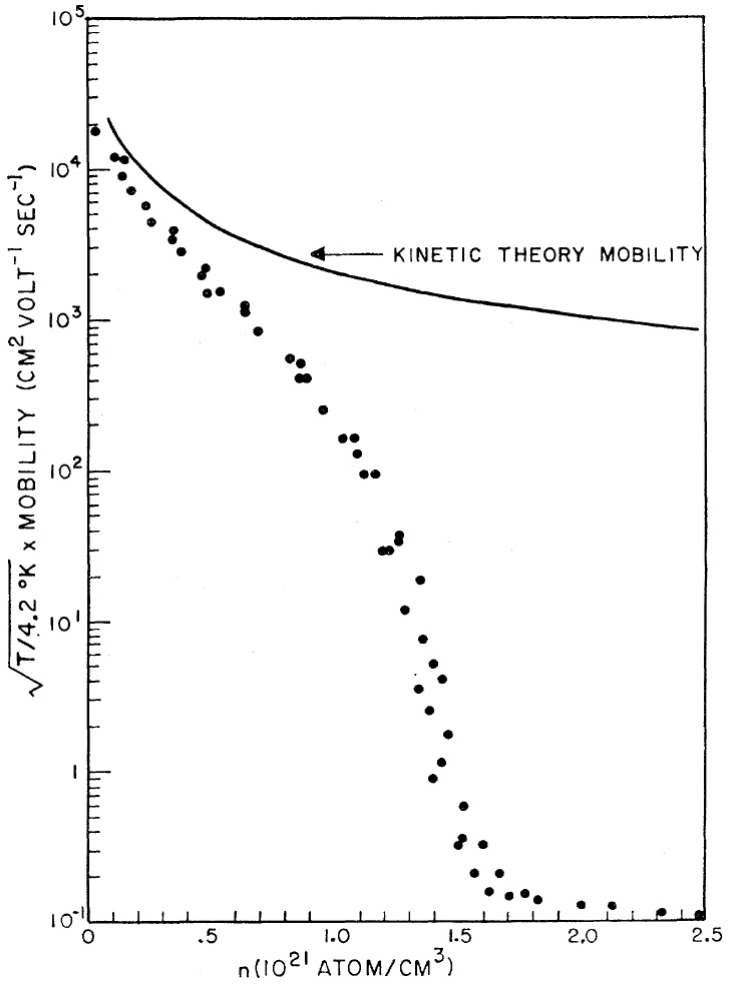

Figure 2-10. The dependence of mobility of electrons in dense helium gas upon gas density.

Figure 2-11 shows the dependence of drift velocity of an electron in dense helium gas. (P_s is the pressure of saturated vapors) [27] In our experiments, the field created by electrodes was $\varepsilon \sim 200$ V/cm. Under these conditions, the drifting

speed of an electron in cold saturated helium gas is ~ 2 Å/ns. If dense helium gas is a good approximation of the properties of not a completely relaxed helium droplet, the motion of the electron under the external electric field is extremely slow on the molecular time scale. This discussion will be continued in the next section.

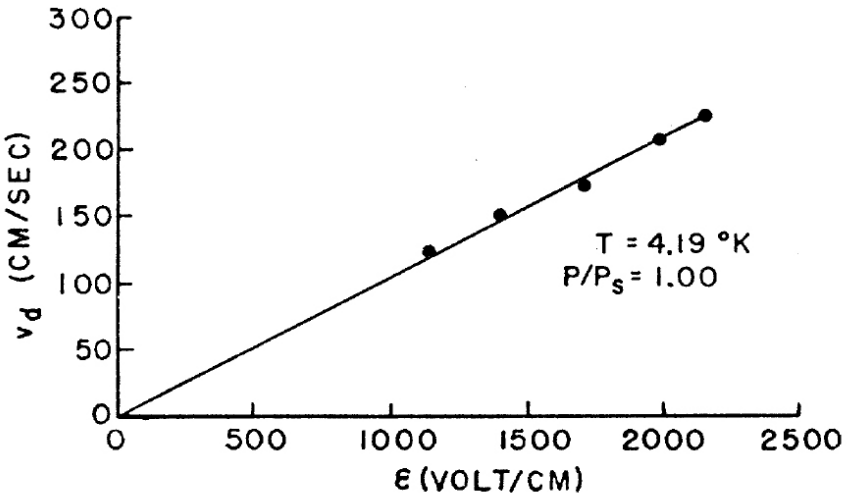

Figure 2-11. Drift velocity of an electron in dense helium gas versus field strength for T = 4.19K.

2.2.3. Escape of electron from helium cluster

It is interesting to consider the properties of an electron bubble approaching the surface of a helium droplet. It has been found that the surface acts as a small potential barrier of ~ 25 cm^{-1} [28] to the extraction of the electron from the liquid to the gas phase. Ancilotto and Toigo [18] investigated properties of electron bubbles close to the surface in the bulk liquid helium. They found that if the electron–surface distance is larger than 23 Å, the bubble is stable. For smaller

distances, the bubble becomes unstable and bursts. They also found that close to the surface the potential of a localized electron (solid line, Fig. 2-12) deviates from the ideal image charge potential, (dashed line, Fig. 2-12). In the absence of an external electric field, the dominant bubble decay mechanism is the tunneling of the electron through the surface layer.

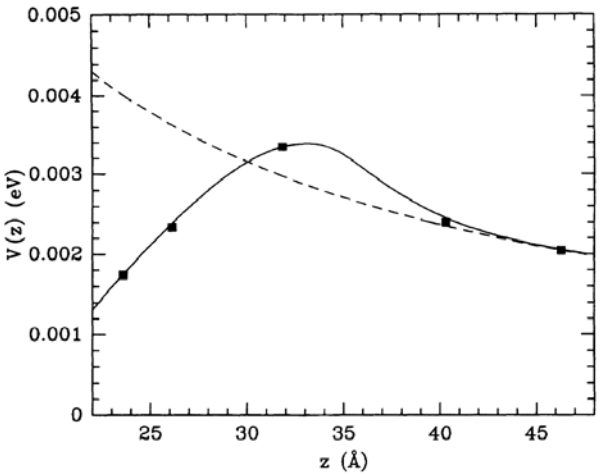

Figure 2-12. Bubble potential energy curve near the surface of liquid helium.

Considering the escape of an electron from the helium cluster, first, it is interesting to know what the liquid-gas interface looks like. Electron is believed to form a spatially localized state inside a dilation of the fluid. The nature of this state is not yet completely understood. The electron can form a bubble, as in the case of liquid helium described above. On the other hand, the electron can be localized in the Anderson sense. In the latter case, the wave function of the electron decays exponentially with the distance due to multiple scattering induced by the disorder of the medium. [26] Theoretical work by Chin and Krotscheck

[29] predicted the thickness of surface region to be about 6 Å. The density of helium in the middle of the droplet is close to its liquid phase value $\rho = 0.022$ Å^{-3}, whereas in the surface region the density drops from 90% to 10% of ρ.

Several works were devoted to the study of electrons embedded in large helium droplets. Toennis and coworkers demonstrated [30] that the electron is unstable in droplets of less than $N = 10^5$.The surface states were predicted to be bound theoretically; the lifetime of this surface state is expected to be less than a nanosecond for an external field of 100 V/cm. One the other hand, electron can form a bubble inside the droplet. The configuration of external and internal states of an electron is sketched in Fig. 2-13 (Adapted from ref [31])

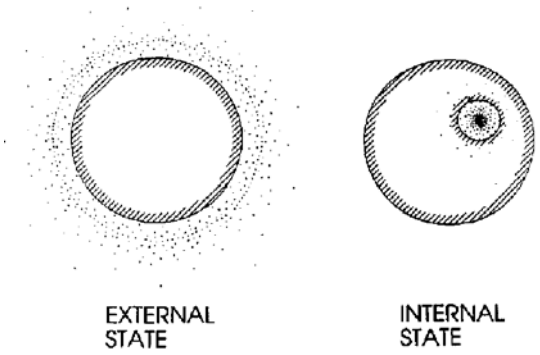

Figure 2-13. Sketch of external and internal states of an electron in a droplet.

Toennies et al. [30] found that the lifetime of an electron lies between 2×10-3 and 2 s (Fig. 2-14). For this reason, the electron is believed to be localized in the interior of the droplet. The threshold of bubble formation was found to be 1.29 eV [32] (kinetic energy of the electron). This value is higher than the barrier of 1.15

eV; therefore, the electron needs additional energy ~ 0.14 eV to penetrate inside the droplet and be captured.

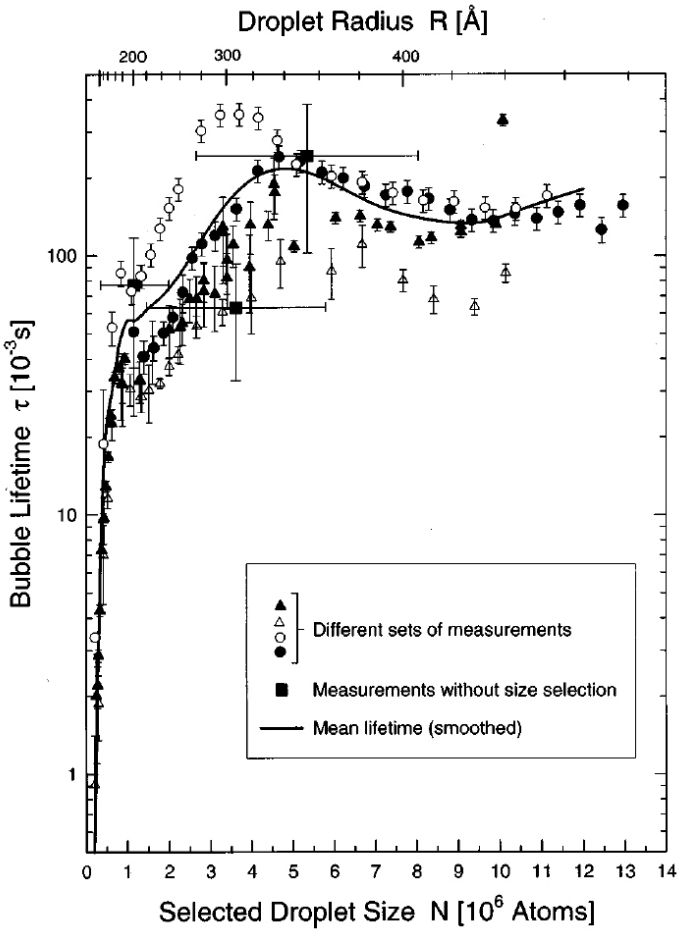

Figure 2-14. Bubble life time in helium clusters as a function of droplet size

For electron energies higher than ~ 5 eV, the production of negatively charged clusters becomes inefficient, which can be explained by the fact that droplets with $R \leq 500$ Å can not dissipate all the energy, and the electron flies through the droplet. To complete that picture, one can mention that the capture of

electrons with E_{kin} > 20 eV is possible due to electronic excitation of helium atoms. The bubble life time does not depend significantly on the initial electron energy.

It is interesting to note that the smallest droplet that can accommodate an electron has diameter of ~ 100 Å. This is in agreement with the calculations of Ancilotto and Toigo [18] described above. The lifetime of a bubble inside a helium droplet can be changed by the presence of foreign species in the droplet. [33] Small closed-shell molecules, such as SF_6, O_2, and small clusters of H_2O, were found to bind an electron and protect it from spontaneous ejection. In contrast, rare gas atom and small clusters do not attach to the electron, pushing the electron away and closer to the surface.

2.3. Interaction of helium with positive impurities

It is known from the mobility studies of liquid helium in the early 70's that helium forms a solid-like cluster or a "snowball" around a positive ion. This snowball contains 30-50 helium atoms and has the diameter of 12 Å. [34-36] The Atkins model treats helium around a positive center as a "continuous" sphere [34], which is oversimplification. Namely, in contrast with the predictions of the Atkins model, ion mobility depends on the atomic number in a way that cannot be explained simply in terms of the mass of the ion. [37]

Only quantum calculations treating helium around positive ions as a discrete atomic shell can predict realistic properties of snowballs. For instance,

recent theoretical studies by Nakayama and Yamashita employed the path integral Monte Carlo method to study the microscopic structure of Na^+-helium clusters. [38] They found that these clusters for N > 100 have a triple-layer structure.(See Fig. 2-15) The first solvation shell is solid-like, the second shell is partially solidified, and the third one is close to liquid helium.

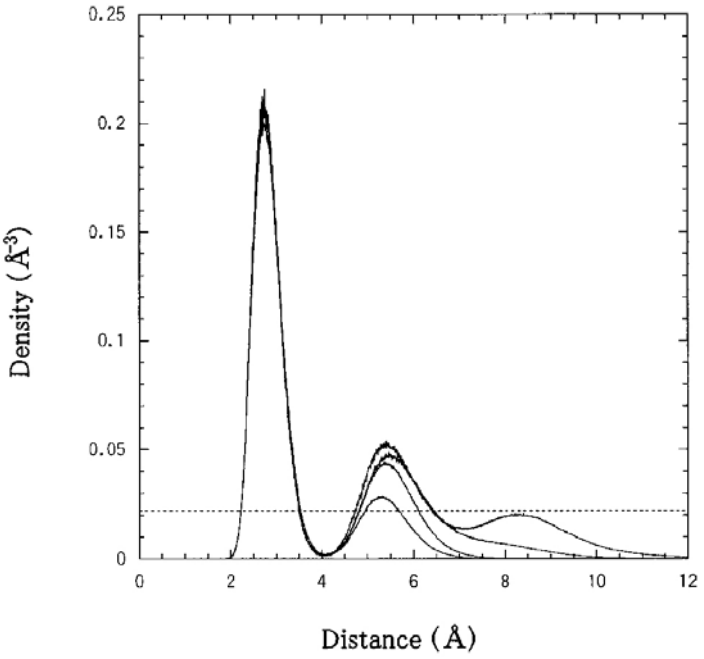

Figure 2-15. Helium density profiles for the Na^+-He_N clusters at T= 1.0 K. The origin is set to be the position of Na^+. The number of helium atoms is 30, 40, 60, and 100 starting from the curve with the lowest amplitide. The bulk liquid density is indicated by dashed line.

On the other hand, it is almost impossible to build a general model for snowball microscopic structure. The radial density profiles found by Reatto et al. [39] show that the microscopic structure of the snowball is remarkably varied for

different ions. In all cases, the first shell of He atoms is ordered, but only in the case of Na^+ and K^+ are the atoms of the first shell essentially localized such that the snowball can be considered a solid. In the case of Li^+ and Cs^+ these He atoms readily exchange with others, and this difference shows up dramatically in the values of the effective masses.

2.4. Location of species in helium droplets

In the case of helium droplets, the strength of the helium-impurity interaction determines not only the configuration of the helium around the impurity but also the position of the molecule inside or on the surface of the droplet. Weak forces of vdW attraction, Pauli repulsion, and surface tension determine the chemical potential of the molecule inside the helium. The location of the impurity can be estimated the from impurity-He potential ε predicted by the model proposed by Ancilotto et al. [40] This model proposes that solvation can be predicted by comparison of the gain in energy due to the interaction between the impurity species and helium against the cost in energy required for creating a cavity within the liquid helium. The dimensionless parameter λ is predicted to be less than 1.9 if the impurity residues on the surface, while dopants with $\lambda > 1.9$ are solvated.

$$\lambda = 2^{-\frac{1}{6}} \frac{\rho \varepsilon r_e}{\sigma} \qquad (2.8)$$

where σ is the surface tension of the liquid helium (0.179 cm^{-1} $Å^2$), and r_e is the equilibrium bond distance for helium-impurity pair interaction.

For most closed-shell molecules, the well depth for helium-impurity,ε, lies in the region 50 - 100 cm^{-1}. [41] Experimental and theoretical studies have shown that for a vast majority of molecules, vdW complexes and non-metallic atoms in a ground state reside in the middle of the droplet. In contrast, the He-alkali atom interaction potential is very weak ($\varepsilon < 1.5 cm^{-1}$). The size and shape of the helium surface around the alkali atom in general is determined by interaction of metal atom electron and helium, which can be described with the help of the "bubble" model, though bubble diameter is smaller than for a free electron. Alkali atoms and their clusters are believed to form a "dimple" structure on the surface of a droplet. [41] For example, an Ag atom in its ground state is resides inside the droplet. Federmann et al. demonstrated that an electronic excitation causes the extraction of the Ag atom from the droplet. [42] The next question is localization of the molecule with respect to the center of the droplet. Lehmann, considered a helium droplet as a dielectric sphere and found that due to induction forces, positive ions are localized near the center of the helium cluster, with the root mean squared displacement of a few Å. [43]

2.5. Ionization in helium droplet

There are two major ways to ionize an impurity on the surface or inside helium droplets. First, positive ions can be formed as a result of electron

bombardment ionization. Second, an impurity can be directly ionized by one or several photons. The aim of this section is to compare these two ionization techniques. Let us consider the mechanism of electron bombardment ionization (Fig. 2-16). This can be considered as four independent consecutive steps [44-48] (The electron energy is above the helium ionization potential 24.59 eV). Although the ionization mechanism described above is oversimplified, it provides a qualitative microscopic picture.

The incident electron ionizes a single helium atom in the vicinity of the droplet surface. This charge delocalizes via resonant hoping charge transfer. According to Halberstadt and Janda [49], resonant charge transfer is an extremely fast mechanism with a mean time between steps of ~ 20 fs. Motion of the charge can terminate if it collides with an impurity or combines with a neutral helium atom to form He_2^+. Association of He_2^+ releases 2.35 eV into the helium bath inducing the fragmentation of the droplet. Moreover, localization of a positive charge on an impurity leads to the release of 8 - 17 eV, which is sufficient to evaporate a significant percentage of the droplet.

Usually the binding energy of a X^+ - He (X is a molecule or atom) binary complex is much stronger than the binding energy of the corresponding neutral X - He complex. Therefore, the surrounding helium atoms will be attracted to the ionic center, providing more energy for cluster fragmentation.

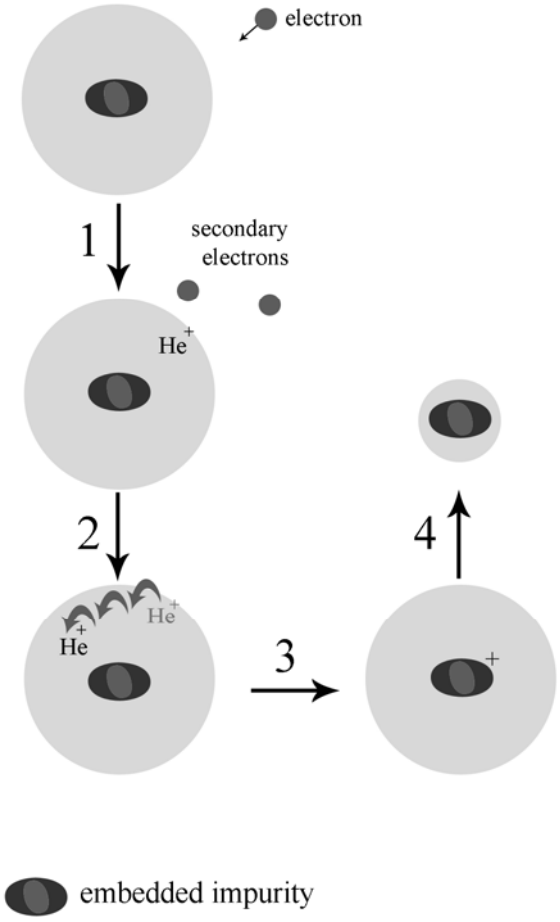

Figure 2-16. Schematic diagram of the mechanism of electron bombardment ionization

Step 4 leads to formation of a progression of He_n^+ clusters where *n* can exceed 100. A typical example of the mass spectrum of pure a helium cluster is shown in Fig. 2-17. He_2^+ is always the main channel of droplet fragmentation. The appearance of "magic numbers" in fragmentation patterns relates to the stability of the fragment ions, as opposed to the stability of neutral cluster precursors before ionization. It is worth noting that the fragmentation pattern is

similar for a broad range of initial cluster sizes. Namely, the probability of detection of small clusters remains large even when the initial neutral cluster size is large. ($N > 10^5$-10^7) In a pure helium droplet the internal energy of a He_N^+ cluster is efficiently transferred to the nearby helium bath, which is believed to facilitate ejection of the ionic clusters.

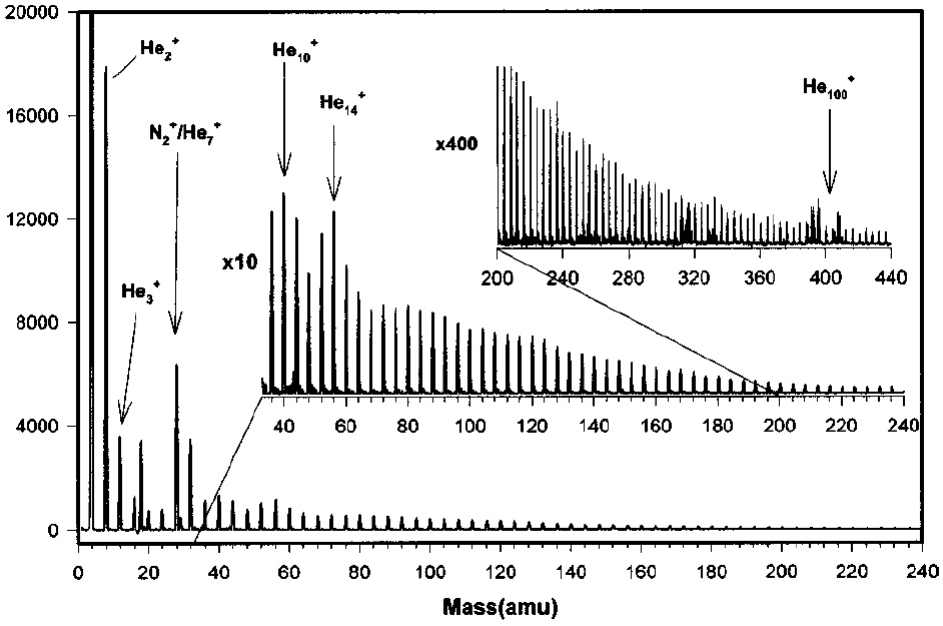

Figure 2-17 Mass spectrum of pure helium clusters with <*N*> = 15000

In contrast, for doped clusters the probability of charge transfer from He^+ to the impurity depends strongly upon the size of the initial droplet. If more than one molecule or atom is embedded in the initial cluster, it is important to know if ionization preserves the original cluster or if the fragmentation of the impurity cluster takes place.

An intriguing question is the mechanism of ejection of small positive clusters. Several hypotheses are available, but none provides a complete picture. Below is a brief description of these models:

- Ovchinnikov's hypothesis [50]: He_3^+, a stable ion with a linear structure, is believed to be a "relaxation kernel". In particular, first He_2^+ starts to form. When two helium atoms are close enough, a potential well is created for a third helium atom at either end of the He_2^+. During subsequent expansion of the initial He-He bond, the third helium atom is strongly attracted to the charged center. Later, one of the two initial helium atoms is ejected with considerable kinetic energy.

- Gspann et al. hypothesis [51]: The ejection of small clusters is due to heating of the temporary depleted zone between the electrostrictively compressed ion vicinity and the undisturbed helium bath. The ejection of small positive cluster is much faster than thermal relaxation.

- Ejection of species formed close to the surface: Haeften et al. [52] reported desorption of atoms in electronically excited states from large helium clusters. Depending on the excitation energy, various atomic and molecular electronic states are involved in the relaxation process. With increasing cluster size the intensity of molecular transitions becomes dominant. The temperature of ejected molecules could be estimated at $T_{vib} \sim 2500$ K and $T_{rot} \sim 450$ K.

Moreover, Northby et al. found that vibrational excitation induces ejection of previously formed metastable clusters.[53] Small ion clusters are believed to be formed in the vicinity of the droplet surface. Overall, the detail mechanism of snowball formation and ejection as a result of electron impact ionization is not yet understood.

Recently, Farnik and Toennies demonstrated an elegant way to initiate ion-molecule reaction by means of electron bombardment ionization. [54] He^+ formed at step 1 of ionization undergoes charge transfer with embedded D_2, N_2, and CH_4. Later, these secondary reactions were observed:

$$\begin{aligned} N_2^+ + D_2 &\rightarrow N_2D^+ + D \\ CH_4^+ + D_2 &\rightarrow CH_4D^+ + D \\ CH_3^+ + D_2 &\rightarrow CH_3D_2^+ \end{aligned} \qquad (2.7)$$

The existence of these reaction channels is due to efficient charge transfer between embedded species.

The ionization of an impurity by laser or synchrotron radiation is differs from electron bombardment ionization. If the photon energy is below ~ 21 eV, only direct ionization of the impurity is possible. For energies above this value, excitation of the Rydberg states of the helium atom leads to formation of quasistable He_2^+. For energies above helium atomic IP, direct ionization of the helium atom is possible.

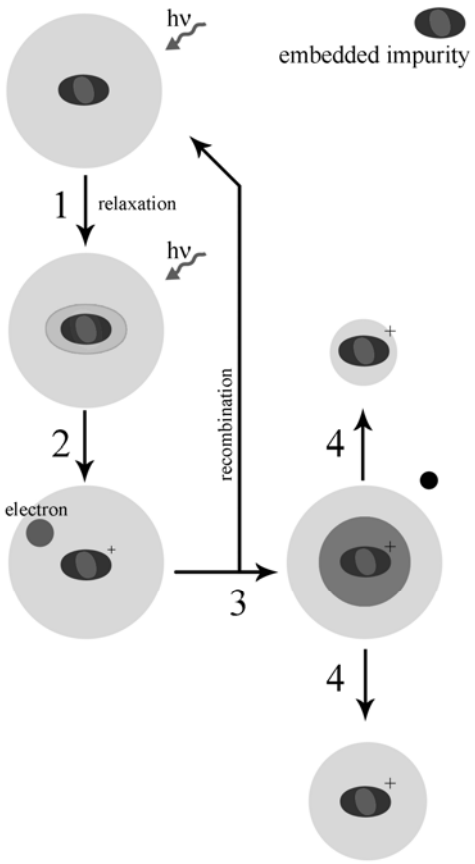

Figure 2-18 Mechanism of laser induced ionization

In the research presented in this thesis, the direct ionization of an impurity by one or multi-photon processes by visible/UV photons is of particular interest. The step-by-step mechanism process is depicted in Fig. 2-18. One or several photons excite an impurity inside the droplet. (It is assumed that one-photon ionization is not possible.) One more photon ionizes the impurity. If there is a time delay between step 1 and step 2, the excited impurity can be involved in a complicated relaxation process. For instance, rotational, vibrational and electronic

relaxation is possible. Moreover, the impurity can move toward the surface of the helium droplet or can even be ejected. As a result of ionization, a positive ion and an electron are formed. The photoelectron's kinetic energy can be efficiently absorbed and dissipated by helium bath, as discussed below and recombination of the ion and electron is possible. Even if the electron is slowed down, it can leave the droplet. If the electron escapes the droplet, two scenarios are possible. First, the impurity or the impurity with a number of helium atoms attached can be ejected/desorbed from the droplet. Second, the impurity can be trapped inside the droplet forming a huge positive cluster.

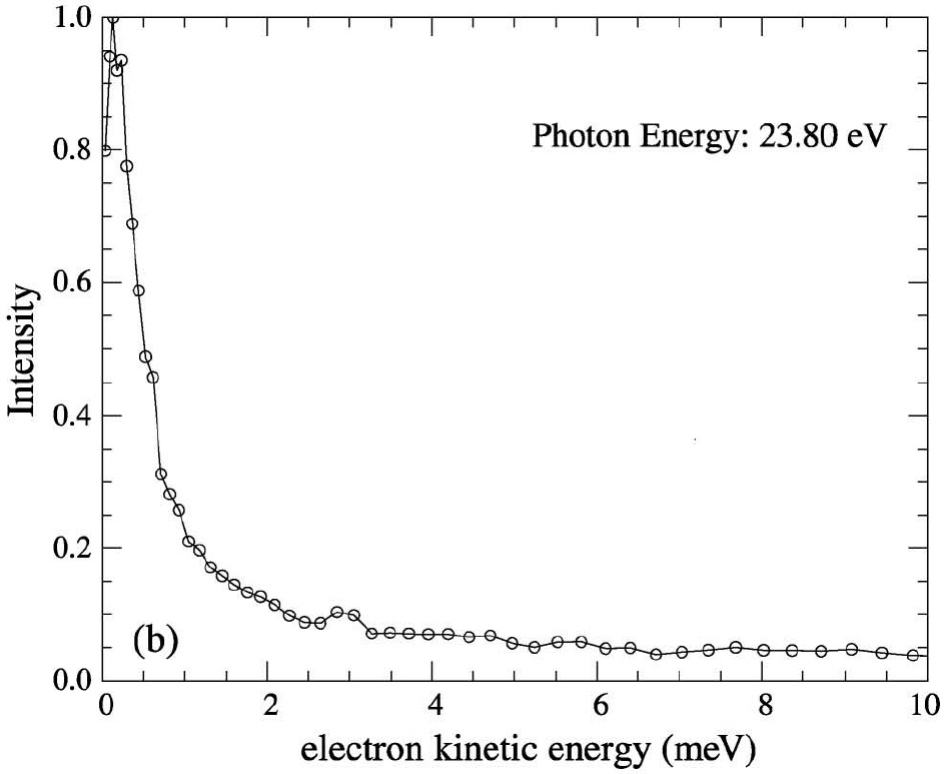

Figure 2-19. Photoelectron energy distribution for a photon energy of 23.8 eV.

Neumark et al. [55] found that photoionization of pure helium droplets by synchrotron radiation (22.5-24.5 eV) results in the formation of extremely slow electrons, i. e. with $<E_{kin}>$ less than 0.6 eV (Fig. 2-19): the formation of these slow electrons is attributed to autoionization of vibrationally excited small helium clusters followed by thermalization of photoelectrons.

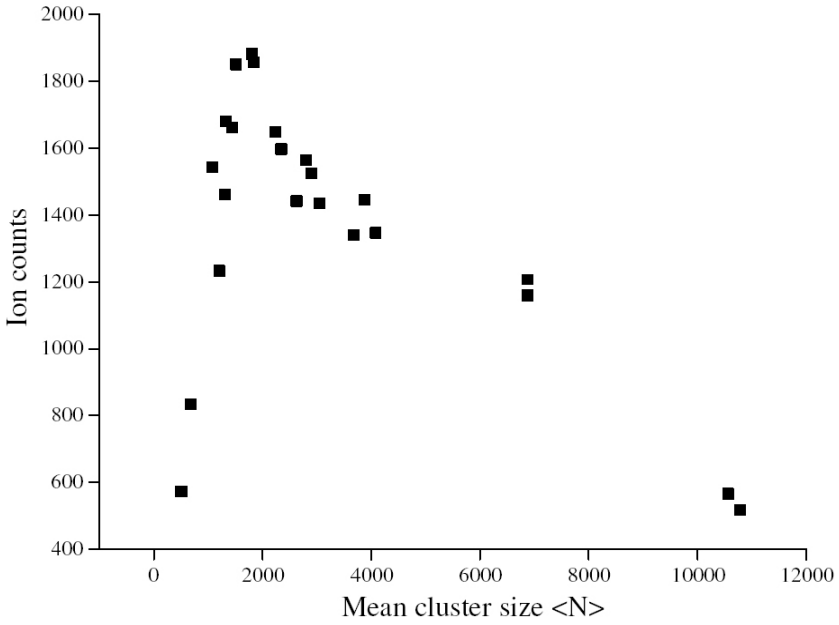

Figure 2-20. Ionization efficiency of benzene at ~ 259 nm as a function of mean size of helium cluster.

Step 3 of ionization can be significantly suppressed in large helium clusters as reported by Stace et al. This effect can be explained by ion-electron

recombination, or the trapping of an ion in the large helium cluster that cannot be detected. [56] Berkeley group reported similar cluster size dependence for NO dimer. [57]

Recently, photoionization of metal clusters has become an active area. The major contribution in this field has been produced by the Meiwes-Broer group. [58-61] Fragmentation of clusters of magnesium, lead and silver have been investigated in detail, but the dynamical picture of ionization is not yet complete.

2.6. References

1. Onnes, K., Commun. Phys. Lab. Leiden. 1908. **105**: 744.

2. Becker, E.W., Z. Phys. D., 1986. **3**: 101.

3. Toennies, J.P. and A.F. Vilesov, Annu Rev Phys Chem. 1998. **49**: 1.

4. Buchenau, H., E.L. Knuth, J. Northby, J.P. Toennies, and C. Winkler, J Chem Phys. 1990. **92**(11): 6875.

5. Jiang, T. and J.A. Northby, Physical Review Letters. 1992. **68**(17): 2620.

6. Slipchenko, M.N., S. Kuma, T. Momose, and A.F. Vilesov, Rev Sci Instrum. 2002. **73**(10): 3600.

7. Grisenti, R.E. and J.P. Toennies, Physical Review Letters. 2003. **90**(23).

8. Toennies, J.P. and A.F. Vilesov, Angew Chem Int Edit. 2004. **43**(20): 2622.

9. Harms, J., J.P. Toennies, and F. Dalfovo, Phys Rev B. 1998. **58**(6): 3341.

10. Gough, T.E., M. Mengel, P.A. Rowntree, and G. Scoles, J Chem Phys. 1985. **83**(10): 4958.

11. Levis, R.J., Annu Rev Phys Chem. 1994. **45**: 483.

12. Claas, P., S.O. Mende, and F. Stienkemeier, Rev Sci Instrum. 2003. **74**(9): 4071.

13. Stein, G.D., Surf Sci. 1985. **156**(JUN): 44.

14. Harms, J., M. Hartmann, J.P. Toennies, A.F. Vilesov, and B. Sartakov, J Mol Spectrosc. 1997. **185**(1): 204.

15. Lewerenz, M., B. Schilling, and J.P. Toennies, J Chem Phys. 1995. **102**(20): 8191.

16. Shikin, V.B., Usp Fiz Nauk+. 1977. **121**(3): 457.

17. Northby, J.A. and T.M. Sanders, Physical Review Letters. 1967. **18**: 1184.

18. Ancilotto, F. and F. Toigo, Phys Rev B. 1994. **50**(17): 12820.

19. Ostermeier, R.M., Physical Review A. 1973. **8**: 514.

20. Ellis, T., P.V.E. Mcclintock, and R.M. Bowley, J Phys C Solid State. 1983. **16**(15): L485.

21. Springett, B.E., Physical Review. 1967. **155**: 139.

22. Rosenblit, M. and J. Jortner, Physical Review Letters. 1995. **75**(22): 4079.

23. Jiang, T., C. Kim, and J.A. Northby, Physical Review Letters. 1993. **71**(5): 700.

24. Borghesani, A.F. and M. Santini, Phys Rev E. 2002. **65**(5).

25. Polischuk, A.Y., J Phys B-at Mol Opt. 1983. **16**(20): 3853.

26. Omalley, T.F. and R.W. Crompton, J Phys B-at Mol Opt. 1980. **13**(17): 3451.

27. Levine, J.L. and T.M. Sanders, Physical Review. 1967. **154**(1): 138.

28. Schoepe, W. and C. Probst, Phys. Lett. A. 1970. **34**: 490.

29. Chin, S.A. and E. Krotscheck, Phys Rev B. 1995. **52**(14): 10405.

30. Farnik, M., B. Samelin, and J.P. Toennies, Journal of Chemical Physics. 1999. **110**(18): 9195.

31. Northby, J.A., C. Kim, and T. Jiang, Physica B. 1994. **197**(1-4): 426.

32. Henne, U. and J.P. Toennies, J Chem Phys. 1998. **108**(22): 9327.

33. Farnik, M. and J.P. Toennies, J Chem Phys. 2003. **118**(9): 4176.

34. Atkins, K.R., The Physical Review. 1959. **116**(6): 1339.

35. Cole, M.W. and R.A. Bachman, Physical Review B. 1977. **15**(3): 1388.

36. Foerste, M., H. Guenther, O. Riediger, J. Wiebe, and G.Z. Putlitz, J Low Temp Phys. 1998. **110**(1-2): 231.

37. Glaberson, W.I. and W.W. Johnson, J Low Temp Phys. 1975. **20**(3-4): 313.

38. Nakayama, A. and K. Yamashita, J Chem Phys. 2000. **112**(24): 10966.

39. Buzzacchi, M., D.E. Galli, and L. Reatto, Physical Review B. 2001. **6409**(9).

40. Ancilotto, F. and P.B. Lerner, J. Low Temp. Phys. 1995. **101**: 1123.

41. Stienkemeier, F. and A. Vilesov, J. Chem. Phys., 2001. **115**(22): 10119–10137.

42. Federmann, F., K. Hoffmann, N. Quaas, and J.D. Close, Physical Review Letters. 1999. **83**(13): 2548.

43. Lehmann, K., Mol. Phys., 1999. **97**: 645.

44. Ruchti, T., B.E. Callicoatt, and K.C. Janda, Phys Chem Chem Phys. 2000. **2**(18): 4075.

45. Ruchti, T., K. Forde, B.E. Callicoatt, H. Ludwigs, and K.C. Janda, J Chem Phys. 1998. **109**(24): 10679.

46. Callicoatt, B.E., K. Forde, L.F. Jung, T. Ruchti, and K.C. Janda, J Chem Phys. 1998. **109**(23): 10195.

47. Callicoatt, B.E., K. Forde, T. Ruchti, L.L. Jung, K.C. Janda, and N. Halberstadt, J Chem Phys. 1998. **108**(22): 9371.

48. Callicoatt, B.E., D.D. Mar, V.A. Apkarian, and K.C. Janda, J Chem Phys. 1996. **105**(17): 7872.

49. Halberstadt, N. and K.C. Janda, Chem Phys Lett. 1998. **282**(5-6): 409.

50. Ovchinnikov, M., B.L. Grigorenko, K.C. Janda, and V.A. Apkarian, J Chem Phys. 1998. **108**(22): 9351.

51. Gspann, J. and H. Vollmar, J Low Temp Phys. 1981. **45**(3-4): 343.

52. von Haeften, K., A.R.B. de Castro, M. Joppien, L. Moussavizadeh, R. von Pietrowski, and T. Moller, Physical Review Letters. 1997. **78**(23): 4371.

53. Northby, J.A., S. Yurgenson, and C. Kim, J Low Temp Phys. 1995. **101**(3-4): 427.

54. Farnik, M. and J.P. Toennies, J Chem Phys. 2005. **122**: 014307.

55. Peterka, D.S., A. Lindinger, L. Poisson, M. Ahmed, and D.M. Neumark, Physical Review Letters. 2003. **91**(4).

56. Curtis, S., A. Boatwright, R.R. Wright, and A.J. Stace, Chem Phys Lett. 2005. **401**(1-3): 254.

57. Peterka, D.S. and D.M. Neumark. 2005.

58. Doppner, T., S. Teuber, T. Diederich, T. Fennel, P. Radcliffe, J. Tiggesbaumker, and K.H. Meiwes-Broer, Eur Phys J D. 2003. **24**(1-3): 157.

59. Diederich, T., J. Tiggesbaumker, and K.H. Meiwes-Broer, J Chem Phys. 2002. **116**(8): 3263.

60. Doppner, T., T. Diederich, J. Tiggesbaumker, and K.H. Meiwes-Broer, Eur Phys J D. 2001. **16**(1-3): 13.

61. Radcliffe, P., A. Przystawik, T. Diederich, T. Doppner, J. Tiggesbaumker, and K.H. Meiwes-Broer, Physical Review Letters. 2004. **92**(17).

Chapter 3: Experimental Apparatus

3.1. Vacuum system

As part of this work a new helium droplet beam machine has been built and made operational in our lab. Fig. 3-1 A shows a photo of the helium droplet machine; the same experimental arrangement is depicted schematically in Fig. 3-1 B. The vacuum system consists of four separately pumped chambers. Going from left to right in Fig. 3-1 B, the helium droplet source is located in the first chamber, which is labeled I. The helium droplets are produced by the expansion of gaseous helium (Spectra Gases, 99.9999%) through a 5μm nozzle (labeled 2) that is attached with a copper braid to a closed cycle helium refrigerator 1b (Advanced Research Systems). The detailed design of the cryogenic source and nozzle is given in the next two sections. Before arriving at the nozzle, the helium is "pre-cooled" by passage through a heat exchanger that is attached to another closed cycle refrigerator 1a (CTI Cryogenics). The temperature of the pre-cooling stage is below 30 K. This arrangement enables the nozzle temperature to be maintained at 14.5 K. The cryogenic nozzle 2 and the second stage of the refrigerator 1b are protected from radiation by a copper shield attached to the first stage of the refrigerator 1b. Temperatures were measured by using a silicon diode sensor.

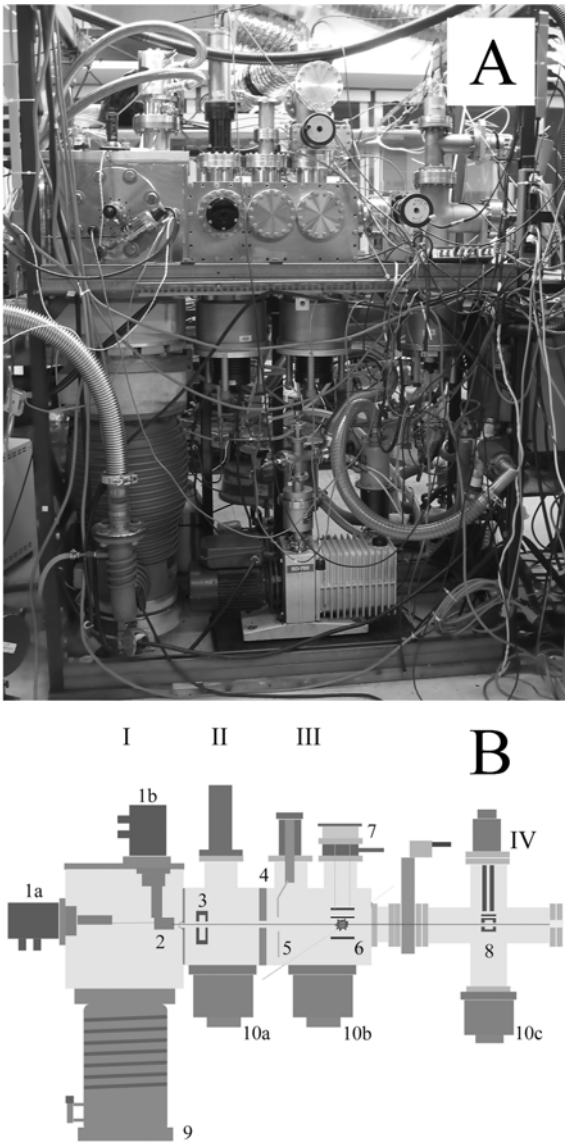

Figure 3-1. A – Photograph of the helium droplet machine, B- Schematic diagram of the experimental apparatus, I. Helium droplet source chamber, II. pickup chamber, III. detection chamber, IV. quadrupole mass-spectrometer chamber. 1a,b –closed cycle refrigerators, 2 – nozzle, 3 – pickup cell 4 – cold finger, 5 – copper plate, 6 – set of electrodes, 7 – MCP (microchannel plate),8 – quadrupole mass-spectrometer, 9 – diffusion pump, 10 a,b,c – turbo-molecular pumps.

The pressure of the helium behind the nozzle can be adjusted by a regulator (Matheson 3510, CGA-580) at the range 5-55 bar. For the experiments described in Chapter 5, the pressure used is 50 bar, which corresponds to a mean cluster size of $\overline{N} \sim 11{,}000$ (See Fig. 2-2).

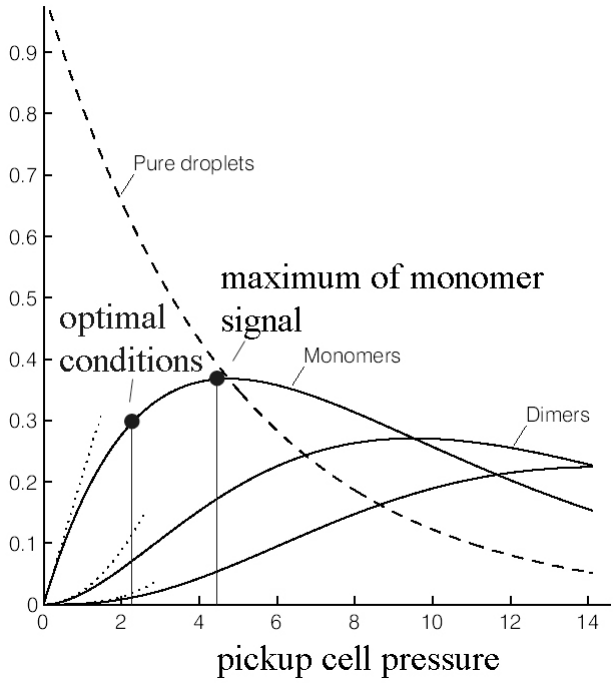

Figure 3-2. Plot of the relative intensities of monomers, dimers and pure droplets.

After passing through a 400 μm skimmer (Beam Dynamics), the droplets enter chamber II, where they pass through a pickup cell (labeled 3) containing NO (Matheson, CP grade, 99%, used without purification) or NO_2 (Matheson, 99%) that is located 10 cm downstream from the nozzle. The pressure of the second

chamber was monitored a by Granville-Phillips micro iongauge during our experiments. The degree of doping was regulated by a bellows-sealed metering needle valve (Swagelok).

For all of the experiments described herein, the regime "1 droplet-1 dopant molecule" was enforced. Figure 3-2 represents a simple qualitative method to find the optimal experimental conditions for this regime. As can be derived from equation (2.3), at the maximum of the monomer signal about 10% of all droplets will be doped by dimers. For this reason, the pressure, which corresponds to ~ 70% of the maximum signal of the monomer, was found to be the optimal parameter. At this pressure, the peak that corresponds to the impurity dimer barely appears in the mass spectrum that is recorded by using the quadrupole mass spectrometer (labeled 8, Blazers) located in chamber IV. Thus, most of the signal originates from the droplets that contain a single molecule.

For some molecules, a correction must be done for the fragmentation of impurity clusters during the electron bombardment ionization. Moreover, the fragmentation ratio depends strongly upon cluster size. [1] This fact must be taken into account for characterization of the doped helium beam. For example, for small helium droplets the ionization by electron impact of a droplet doped by two NO molecules result in the formation of $(NO \cdot He_m)^+$ progression; no $([NO]_2 \cdot He_n)^+$ signal was detected.

Another seminal example is a helium droplet doped by noble gas atoms. Ionization of a large helium cluster containing a single Ar atom rarely results in fragmentation to yield Ar^+. Instead, it has been shown that ionization of such clusters yields a broad distribution of He_mAr^+ fragments, in which values of n greater than 50 are readily observed. In contrast, if the neutral cluster contains two Ar atoms, the most probable fragment is Ar_2^+. [1, 2] For organic molecules fragmentation is minor and can be neglected in most cases.

After leaving the pickup chamber (II), the doped helium droplet beam enters the detection chamber (III), which is pumped separately and is separated from the pickup chamber by a 5 mm diameter diaphragm. We built a time-of-tlight mass spectrometer in the chamber. (A detailed description of this spectrometer is available in the section devoted to ion optics). This mass spectrometer detects the ions formed after ionization by laser radiation, and a multi channel plate detector is employed for ion registration.

To protect the active surface of the MCP detector from possible contamination and damage, precautions must be taken. First, the detector cannot be stored on a shelf or in a desiccator for more than one hour. In our machine, the small vacuum chamber with the MCP detector can be separated from the main chamber by a gate valve (Model GV-6000M, MDC).

To minimize the diffusion of gas from the pickup cell into the detection region, a cold copper plate (labeled 5 in Fig 3-1) was introduced; it is connected

with a copper braid to a cold finger that is cooled by liquid nitrogen. The temperature of the copper plate was measured by using a silicon diode.

If the helium machine is to be open to the atmosphere for maintenance, this small chamber must be filled with clean, moisture-free gas (argon or dry nitrogen). Second, one should never apply a high voltage to the MCP detector if the pressure in the MCP chamber is higher than 10^{-6} Torr. Third, the surface of the detector is very sensitive to pump oil. If the MCP chamber is filled with a gas, it is not recommended to pump it out directly by a rough pump even if an oil trap is installed. For this reason, we use a liquid nitrogen trap, which is installed on the top of the rough pump, to eliminate oil backflow into the detection chamber.

Chambers II and III are mainly O-ring sealed, and the front flanges are effortlessly removable, providing easy access to the pick-up cell and TOF mass spectrometer. Unfortunately, there is no valve installed between chambers II and III, and any modification of the machine would require all three chambers to be opened to air. On the other hand, chamber IV is separated from other chambers by a gate valve (Model GV-6000M, MDC Vacuum) and can be pumped out independently. To build this chamber, we used a custom-made four-way cross that is similar to MDC Vacuum item #405006. The mass spectrometer is rigidly attached to one of the flanges of this cross, and the center of the ionization region coincides with the axis of the molecular beam. The helium droplet beam is skimmed and collimated by a molecular beam skimmer and a diaphragm mounted on the internal walls that separate the first three vacuum chambers. An optical

telescope (Nikon AE-7) was used for precise alignment of the helium machine. Appendix A. explains the alignment procedure.

3.2. Cryogenic nozzle design

In the design of the cryogenic nozzle, we utilized the experience of two research groups: Prof. R. Miller's (UNC) and Prof. K. Janda's (UCI). The layout of our cryogenic nozzle is shown in Fig. 3-3. Briefly, the copper disk (2) is attached to the copper nozzle (4). An indium gasket (3) and brass nut (1) are used for sealing. The nozzle (4) is connected to the holder (6) by four screws, and the Teflon washer (5) thermally isolates these two parts. Moreover, small Teflon home-made washers were used to isolate the screws and the copper nozzle. The nozzle holder (6) is a thin-walled stainless steel tube (d = 1/4").

Unfortunately, it is not possible to order a copper nozzle with a 5μm aperture. A round hole of this diameter can be burned by high-power laser; the thickness of the substrate should not exceed 50 μm. In addition, the aperture can be easily clogged by frozen impurities, dust or small particles and must be replaceable. For this reason, we buy disks with an aperture in the middle. (5μm, National aperture) Even though National Aperture offers several different designs of the aperture, only one fits our nozzle. The O.D. of the disk is 3/8" (the thickness of disk is 0.015"), and the O.D. of the thinner internal part is 3/64" (See Fig. 3-3, part 3). If an aperture with a larger O.D. is used, high pressure gas will damage the aperture. The section of the nozzle tip is shown in the Fig. 3-4. The

surface of the copper nozzle (1) must be clean and smooth to ensure good sealing. If the aperture (3) is to be changed, this surface must be cleaned before the installation of a new one.

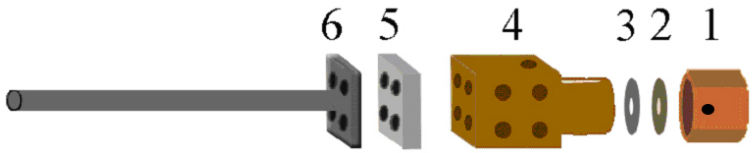

Figure 3-3 Cryogenic nozzle arrangement: 1- brass nut, 2 – aperture, copper disk with 5μm aperture 3 – indium gasket, 4 – copper nozzle, 5 – teflon washer, 6-stainless steel holder

The indium gasket (2) has O.D. ~ 0.3" and I.D. ~ 0.1". These gaskets were made from the indium foil sheets (Lakeshore) with the help of two "cookie-cutters", stainless cylinders with sharp edges. The brass nut (4) has a cone opening on the side of helium expansion.

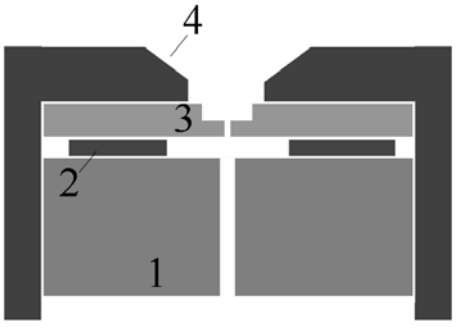

Figure 3-4. Nozzle tip:1 – copper nozzle, 2 – indium gasket, 3 – copper aperture, 4 – brass nut

Without this opening, a region of high pressure would be created close to the nozzle that could cause a severe attenuation of the droplet beam. Once the nozzle is assembled, the sealing must be checked before further assembly of the cryogenic source. The check-up procedure is described in Appendix B.

3.3. Cryogenic droplet source

The cryogenic helium droplet source consists of the nozzle assembly, described in the previous section, helium delivery line, translation XY stage, temperature control system, and radiation shield. Fig. 3-5 shows the design of the XY translation stage. Movable and fixed parts of the setup are thermally connected by means of flexible copper braids (not shown) made of wires of diameter ~ 0.25 mm with free length of 35 mm. One end of the copper braid is fastened to the second stage of the refrigerator, and the other to surface (b) of the nozzle. The silicon sensor diode is attached to surface (a) of the nozzle. The detailed scheme of the silicon sensor assembly is shown in Fig. 3-5. The silicon diode sensor is attached to the surface by the copper custom made, L-shaped washer. An indium foil gasket improves the thermal contact between diode sensor and the body of the copper nozzle. Two terminals of the diode are connected to the temperature controller through cryogenic wires and a vacuum feed-though connector. These wires have low thermal conductivity and relatively high electrical resistivity. Heat flow along the wires can potentially cause temperature misreading. For this reason, the wires are carefully wrapped around the cold head

to increase the wire length between the two refrigerator stages. They are readily secured in place using Teflon tape. A cartridge for resistive heating of the nozzle can be installed on surface (c), Fig 3-5.

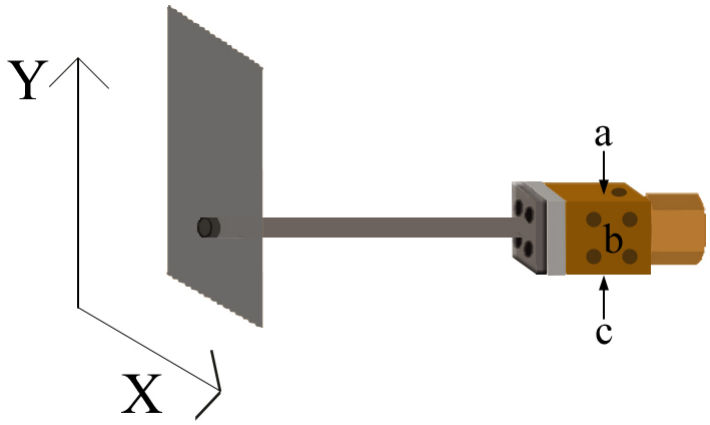

Figure 3-5. XY- motion translational stage. A silicon diode is connected to the surface a of the nozzle, a copper braid – surface b, and helium gas inlet – surface c.

The helium supply line, a copper tube of 1/16" diameter (K&S engineering, McMaster), is connected to the surface of the nozzle that is not visible in Fig. 3-5 via a brass Swagelok 1/16" connector. This connector is welded into the body of the copper nozzle. The stainless nozzle holder is fastened to the aluminum adapter with a screw. (Fig. 3-6) We observed no oscillations of the helium droplet beam intensity due to vibration of the nozzle assembly. Two linear motion stages (Newport, Model 436) were used for control of X and Y position of the nozzle assembly (see Fig 3-5).

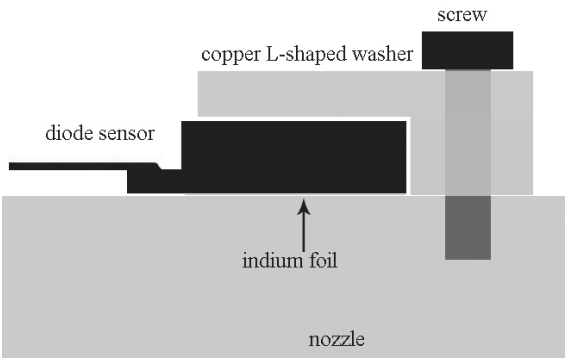

Figure 3-6. Silicon diode sensor assembly

The first stage is attached to the second one, and the second stage is fastened to the aluminum holder affixed to the lid of the vacuum chamber. Micrometers were replaced with aluminum manipulators attached to linear vacuum feedthroughs (MDC Vacuum, 304 Series), so the position of the nozzle could be adjusted from outside the vacuum chamber. The nozzle alignment procedure is explained in Appendix C. The entire cryogenic assembly is protected from black body radiation of the room-temperature walls by a home-made copper shield and several dozen layers of superinsulation (NRC-2, Lakeshore).

3.4. Laser system and optics

For the majority of the experiments presented in this work, a commercial nanosecond laser system (pulse length ~10ns, repetition rate 20 Hz) was used. Briefly, a Nd-YAG laser (Continuum Powerlite 9020) pumps a dye laser (Continuum ND 6000). Typical pulse energies for the Powerlite 9020 laser at 1064 nm and 532 nm are 550 mJ/pulse and 240 mJ/pulse, respectively. The following laser dyes were used to produce laser radiation in the range 542-850

nm: Fluorescein 548, Rhodamine 590, mixture of Rhodamine 590 and Rhodamine 610, Rhodamine 610, mixture of Rhodamine 610 and Rhodamine 640, Rhodamine 640, DCM, LDS 698, LDS 722, LDS 750, LDS 751, LDS 765 and LDS 821 (Exciton). Output energy varied in the range 50-120 mJ.

In general, there are two different way to produce laser radiation in the near UV spectral region. First, the output of the dye laser and residual 1064 nm radiation from second harmonic generation can be mixed inside the UV-extension unit (Continuum UVT-3). Second, the third can be used for pumping of Coumarin dyes. Only the first option was utilized for a number of reasons. Coumarin dyes not only have a short life time (less than one hour), but are also infamous for their poor beam shape. We found that Coumarin dyes are unsuitable for the multiphoton ionization spectroscopy because a non-Gaussian laser beam could not be focused into a small enough spot to obtain the high density of radiation required for non-linear excitation. For this reason, we produced light in the range 365 - 440 nm only by mixing.

Our UVT extension is equipped with a UVT-5 crystal for the generation of light in the region 206 - 220 nm by doubling of dye laser output. Because this scheme necessitates the use of Coumarin dyes, we did not use it. In addition, the design of the UVT extension does not allow doubling after mixing. That is why we mounted non-linear crystal UVT-5 outside of the extension unit and doubled 412 – 440 nm radiation (high quality beam generated by mixing) manually by

adjusting the phase-matching angle of the crystal. Table 3-1 summarizes the methods of light generation that were used in the present work:

Output wavelength, nm	method
206-227	Doubling after mixing
310-365	Doubling
359.5-442	Mixing

Table 3-1. Output of UVT system.

Our lab is equipped with a state-of-the-art picosecond pump-and-probe machine that has been described in detail in our earlier publications. For the current experiment we employed only a small part of this machine, namely, the EKPLA Nd-YAG laser (EKSMA Corp, PL-2143C) and low-vibration mirror mounts. The energy output of the third harmonic is 100 mJ, the repetition rate is 10 Hz, and the pulse duration is ~ 30 ps. However, this machine can be used for a number of promising experiments described in the section devoted to future work. Briefly, two branches of this machine are equipped with tunable distributed feedback dye lasers (DFDL) and an amplifier, and one can generate two channels of visible and UV light.

During the experiment presented in this dissertation, we worked with a broad range of laser light energies, and one of the experimental challenges was to achieve repeatability, day-to-day stability and comparability of data for different

wavelengths. The travel distance of light from the laser to the vacuum chamber is ~ 4 m for the nanosecond system and ~ 8 m for the picosecond one. Moreover, the position of the chamber windows is close to eye-level, and a periscope assembly was built to ensure safety. To propagate the laser beam, we used several different sets of 7 dielectric mirrors (CVI Laser). Quartz prisms, the most popular, universal, and versatile reflectors, are not suitable for the experiments described in this work due to high losses on their surfaces (R < 96%).

The working range (R > 98%) of a dielectric mirror is approximately 10% of the maximum wavelength, and the reflectivity of the mirror is a function of the wavelength. For this reason the laser energy was measured in front of the entrance window of the vacuum chamber. Moreover, a second power meter was utilized to control the energy output behind the vacuum chamber to eliminate influence of power fluctuations on recorded signals; fused silica windows (O.D. = 2", CVI Laser PW-2012-UV) reflect about 10% of radiation for all wavelengths.

The laser beam was focused by a 50 cm lens (Newport, fused silica, KBX082) and it struck the helium-droplet beam halfway between the repeller and extractor electrodes (Section 3.5.). A linear motion stage was used for the fine adjustment of the lens position. It was found that the intensity of the ion current depends strongly on the accuracy of the lens position adjustment (it should be set strictly perpendicular to the laser beam) as well as beam profile quality. To eliminate day-to-day differences in experimental conditions, the procedure described in Appendix D was utilized.

3.5. Time of flight mass spectrometry and data analysis

The ion detection arrangement is shown in Fig. 3-7. It consists of: (a) a set of electrodes; (b) a 75 cm long field-free time-of-flight region; and (c) a microchannel plate (MCP) ion detector (18 mm diameter, BURLE Electro-Optics)

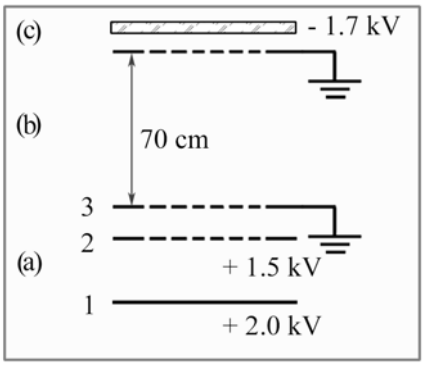

Figure 3-7. Ion detection arrangemen (not to scale): (a) set of electrodes; (b) TOF region; (c) MCP; 1- repeller electrode, 2 – extractor electrode, 3 – grounded shield

There are three electrodes: (1) repeller; (2) extractor; and (3) ground shield. The repeller electrode is a round stainless steel plate 7.5 cm in diameter, while the extractor and shield electrodes have 5 cm diameter fine nickel mesh in their centers. The spacing between the repeller and extractor electrodes is 1.25 cm, and the spacing between the extractor and shield electrodes is 0.625 cm.

Voltages of 2.0 kV and 1.6 kV were applied to the repeller and extractor electrodes. These voltages were optimized to provide the best mass resolution in TOF spectra, *i.e.*, to make the peak corresponded to NO^+ as narrow as possible. The ion detection efficiency of the MCP is about 40% and does not depend

noticeably upon the kinetic energy of the ion. The transmittance of the mesh electrodes is higher than 90%. Fig. 3-8 gives an example of TOF spectrum of a NO embedded in a droplet. Spectrum A shows the TOF in the mass range 0-100 amu. We recorded and added several thousand of TOF spectra together to achieve decent quality. We used the following formula to convert time units (t) into atomic mass units (m):

$$m = \left(t - t_0\right)^2 / a^2 \qquad (3.1)$$

where t_0 = 248.89 and a = 95.76 are parameters found by fitting a TOF spectrum.

The output of the MCP detector is connected to a 12 bit Analog-To-Digital Converter board (CS8012A Gage Applied Science) installed in the experimental computer through a fast amplifier (DC-300MHz Stanford Research Systems). This system allows us to record a TOF spectrum at every laser shot. The temporal resolution of this system is 100 MSamples/sec.

Spectrum B (Fig. 3-8) reveals a potential problem that should be taken into account. After a strong ion flux corresponding to the main product NO+ (*m/Z*=30 amu), the baseline of the MCP signal is distorted, and measurement of the intensities of peaks at masses adjacent to *m/Z*=30 amu can be complicated. The distortion of the baseline can be eliminated by "time gating" the ion flux.

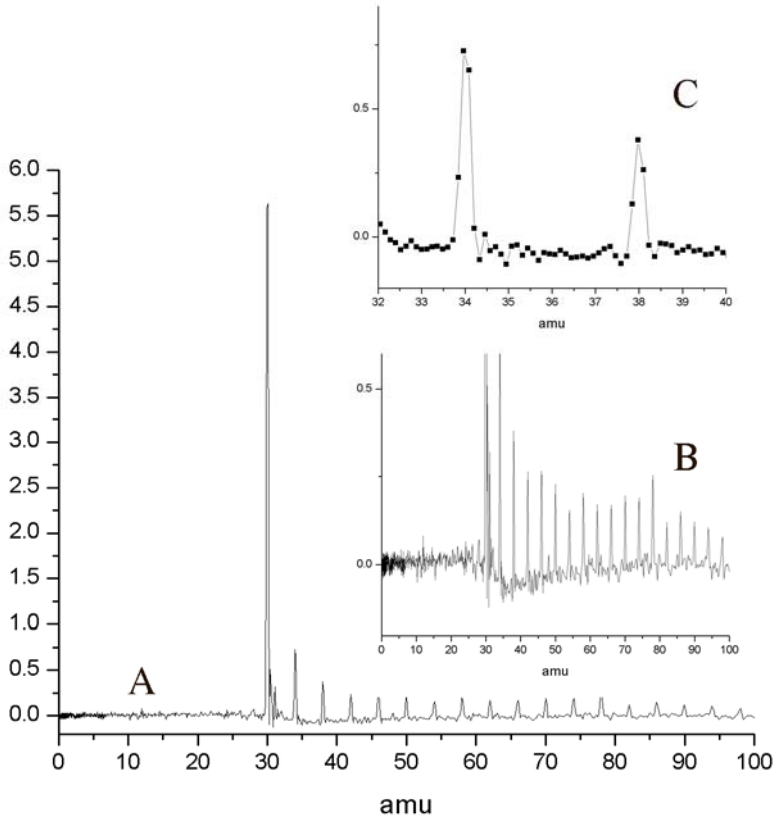

Figure 3-8. Time of flight spectrum of NO embedded in helium droplet. A – full range *m/Z*=0-100 amu, B– the same mass range as in Fig. A but with ×10 vertical scale, C – mass range *m/Z*=32-40 amu.

As one can see from spectrum C, Fig. 3-8, the typical width of the peak corresponding to one particular amu is 40 ns (four points per peak). In this range resolution is 9 points per amu and can easily resolve peaks with $\Delta m = 1$. The finite size and temporal width of the laser pulses are two major factors that contribute to the broadening of the TOF peaks. For every given laser wavelength,

the following procedure was employed to find the intensities of all peaks present in the TOF mass spectrum:

1. At every wavelength we recorded a background TOF spectrum with closed helium-droplet beam and it was subtracted from the TOF spectrum with the helium beam open to eliminate the influence of background NO due to diffusion from the pickup cell.

2. These two spectra were uploaded to a LabView program. Standard FFT filter was used to eliminate high frequency noise and subtract the background spectrum.

3. As a next step, the position of the most intense peak (m/Z = 30 amu) was determined. The positions of all other peaks were calculated with respect to the position of this peak. The intensities of the peaks were found with the help of a standard LabView threshold peak counter routine. Data were normalized and downloaded to a file.

3.6. References

1. Callicoatt, B.E., D.D. Mar, V.A. Apkarian, and K.C. Janda, J Chem Phys. 1996. **105**(17): 7872.

2. Callicoatt, B.E., K. Forde, L.F. Jung, T. Ruchti, and K.C. Janda, J Chem Phys. 1998. **109**(23): 10195.

Chapter 4: NO molecule

The NO molecule has low-lying laser-accessible Rydberg states due to its low ionization potential (74721.7 cm^{-1} [1]), which makes this molecule a perfect candidate for studies of multiphoton ionization of impurities embedded in the helium clusters. The radius of these states is close to or larger than (See Table 4–1 below) the interatomic distance in helium (R_{He-He}= 3.6Å [1]); consequently, one can expect strong Pauli repulsion between the Rydberg electron and closed-shell species. Furthermore, the NO molecule and its complexes have been studied in detail by a variety of experimental techniques. [2] In particular, well-described absorption and fluorescence spectra are available for gas-phase NO, NO·Rg [3] (Rg = rare gas) complexes, and NO trapped inside Rg matrices [4, 5] as well as in H_2 [6] and D_2 matrices [7]. This chapter summarizes experimental and theoretical information on this molecule that is helpful in understanding the experimental results presented in Chapter 5.

4.1. Spectroscopy of NO molecule

Fig. 4-1 shows a diagram of potential energy curves of NO (adapted from ref 2). The energy region investigated in this work is marked as a gray rectangle on this figure. The electronic configuration of NO in its ground state $X^2\Pi$ is $(2p\sigma)^2(2p\pi)^4(2p\pi^*)^1(2p\sigma^*)^0$, and low lying Rydberg states can be excited by

promotion of a single electron positioned on the antibonding 2pπ:

$X^2\Pi \rightarrow A^2\Sigma \qquad (2p\sigma)^2(2p\pi)^4(2p\pi^*)^1(2p\sigma^*)^0 \rightarrow (2p\sigma)^2(2p\pi)^4(2p\pi^*)^0(2p\sigma^*)^0(3s\sigma)^1$

$X^2\Pi \rightarrow C^2\Pi \qquad (2p\sigma)^2(2p\pi)^4(2p\pi^*)^1(2p\sigma^*)^0 \rightarrow (2p\sigma)^2(2p\pi)^4(2p\pi^*)^0(2p\sigma^*)^0(3p\pi)^1$

$X^2\Pi \rightarrow D^2\Sigma \qquad (2p\sigma)^2(2p\pi)^4(2p\pi^*)^1(2p\sigma^*)^0 \rightarrow (2p\sigma)^2(2p\pi)^4(2p\pi^*)^0(2p\sigma^*)^0(3p\sigma)^1$

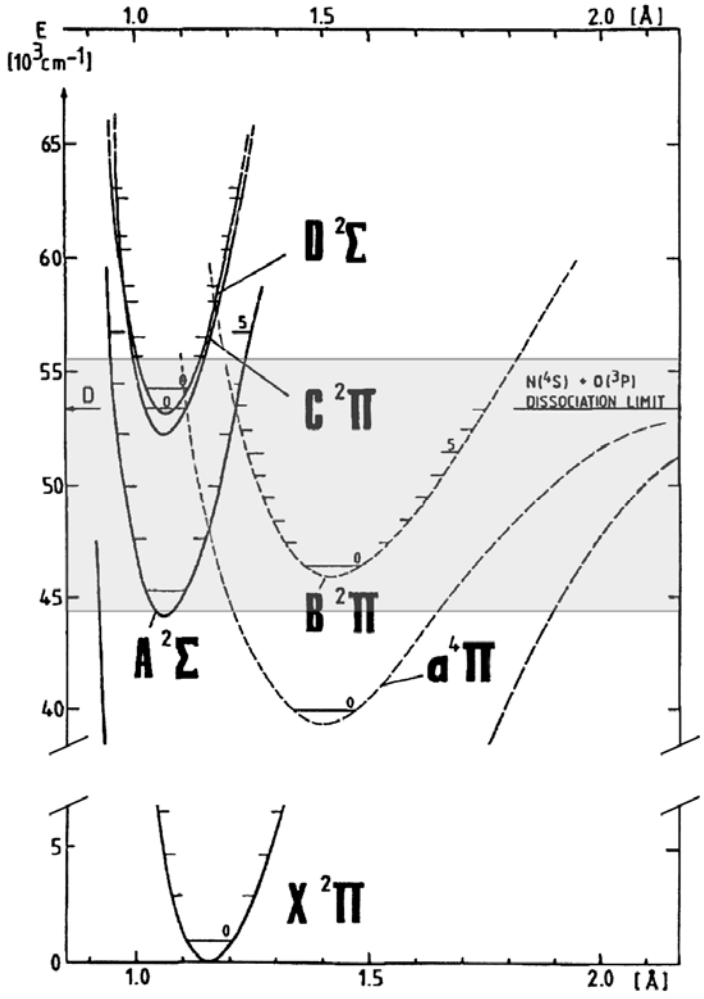

Figure 4-1. Schematic diagram of potential curves of NO.

where $(2p\sigma)^2(2p\pi)^4(2p\pi^*)^0(2p\sigma^*)^0$ is the ionic core NO^+. The interatomic distance of NO^+ (1.06 Å [1]) is close to the geometry of the NO core in the Rydberg state (See Table 4.1); therefore, the Rydberg state can be easily ionized by one-electron excitation:

$$(2p\sigma)^2(2p\pi)^4(2p\pi^*)^0(2p\sigma^*)^1 \rightarrow (2p\sigma)^2(2p\pi)^4(2p\pi^*)^0(2p\sigma^*)^0 + e^- \text{ (For } A^2\Sigma)$$

The ground electronic state of the ion is formed in the same vibrational state as the initially excited intermediate state, while the photoelectron acquires the rest of the energy. The energy of a Rydberg state is given by a well-known Rydberg formula:

$$E_R = E_{ion} - \frac{R_y}{(n-\delta)^2} \qquad (4.1)$$

where R_y is the Rydberg constant, n is a principal quantum number of the orbital, δ is the quantum defect, and E_{ion} is the energy of the ionic state to which the Rydberg series converges. The quantum defect δ reflects the degree of penetration of the Rydberg orbital into the ion core and is primarily defined by the angular momentum of the Rydberg electron. Therefore, each Rydberg state can be distinctively identified and its nature can be determined by obtaining three quantities: E_{ion}, n, and δ. Table 4-1 gives calculated values of T_0, quantum defect, expected Rydberg radius and N-O intermolecular distance for low-lying Rydberg states.

Electronic state	T_0, cm^{-1}	δ	R_{N-O}, Å	$R_{Rydberg}$, Å
$X^2\Pi$	0		1.15077	
$A^2\Sigma$ (3sσ)	44200.2	1.10	1.06434	2.86
$C^2\Pi$(3pπ)	52371	0.78	1.062	3.38
$D^2\Sigma$(3pσ)	53292.4	0.74	1.061	3.52
$E^2\Sigma$(4sσ)	60863.8	1.19	1.064	6.27

Table 4-1. Parameters of low electronic states of NO (from references 1 and 8)

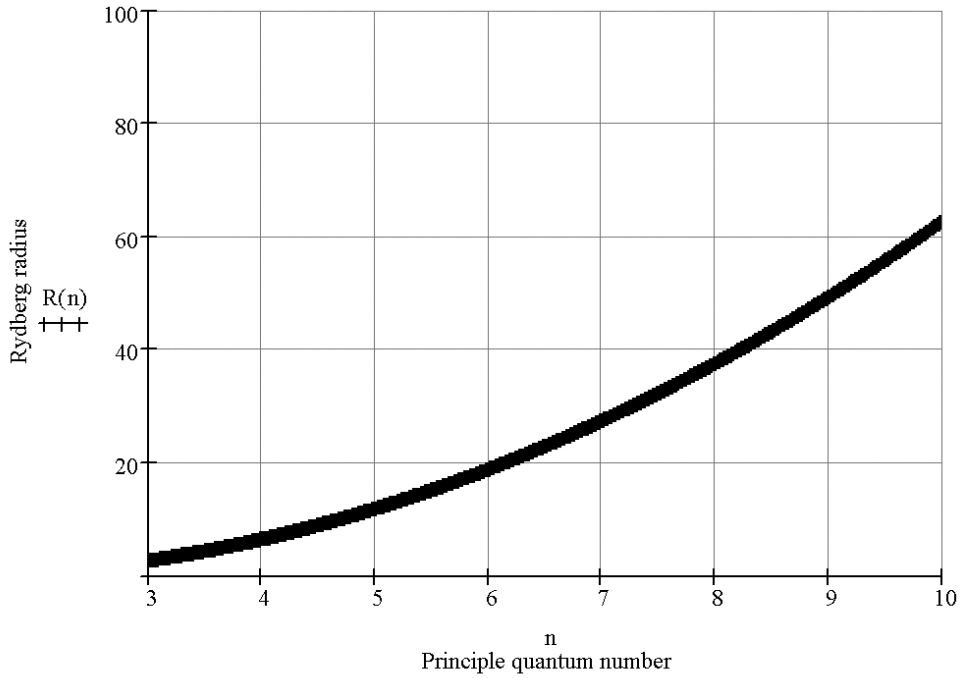

Figure 4-2. Radius of Rydberg orbital (in Ångstroms) as a function of the principle number of this orbital.

The expected radius (maximum of electronic density) of the Rydberg state with high n can be estimated from the formula (4.2):

$$R_{Rydberg}\left(n\right) = R_0 \times 3\left(n-\delta\right)^2 / 2Z \qquad (4.2)$$

where R_0 is the Bohr radius and Z is the nuclear charge. This dependence can be seen in Fig. 4-2 for $\delta = 1.1$; it is noteworthy that for $n > 7$, the size of the Rydberg orbital is comparable to the mean radius of helium clusters used for the experiments described below. The size of the cavities formed when NO is embedded in condensed media is discussed in the next section.

In addition, one can notice that for $n > 3$ the expected values of the Rydberg state is bigger than diameter of helium, and penetration of helium atoms into the ionic core region is possible. (See Section 4-3) Beside the three Rydberg states mentioned above, two valence states, $B^2\Pi$ and $a^4\Pi$, are present in the investigated spectral region. Whereas the $X^2\Pi \rightarrow a^4\Pi$ transition is spin-forbidden, the absorption of $B^2\Pi(\upsilon') \leftarrow X^2\Pi\ (\upsilon''=0)$ band is extremely weak for $\upsilon' < 6$ due to the poor Frank-Condon factors. [8] The ionization cross section of $B^2\Pi$ is significantly lower than that of $A^2\Sigma$ because the ionization of $B^2\Pi$ involves two-electron excitation. [9]

$$(2p\sigma)^2(2p\pi)^3(2p\pi^*)^2(2p\sigma^*)^0 \rightarrow (2p\sigma)^2(2p\pi)^4(2p\pi^*)^0\,(2p\sigma^*)^0 + e^-$$

Although the contribution of valence states into ionization is expected to be negligible, $B^2\Pi$ and $a^4\Pi$ states may be coupled to Rydberg states and play an important role in Rydberg-valence relaxation dynamics.[4, 6] Fortunately, low-

lying vibrational levels (ν'=0-2) of the $A^2\Sigma$ state in the region 45000-50000 cm^{-1} are known to be isolated from valence states. That is why we focused our studies on this particular energy region. The $A^2\Sigma$ state has a spontaneous emission lifetime of 200 ns [10].

4.2. NO trapped in matrices

NO has been used for decades as a probe of the microscopic interaction of an impurity and a low-temperature noble gas matrix. In the context of the current work, the photoinduced rearrangement in many-body systems is of particular interest.

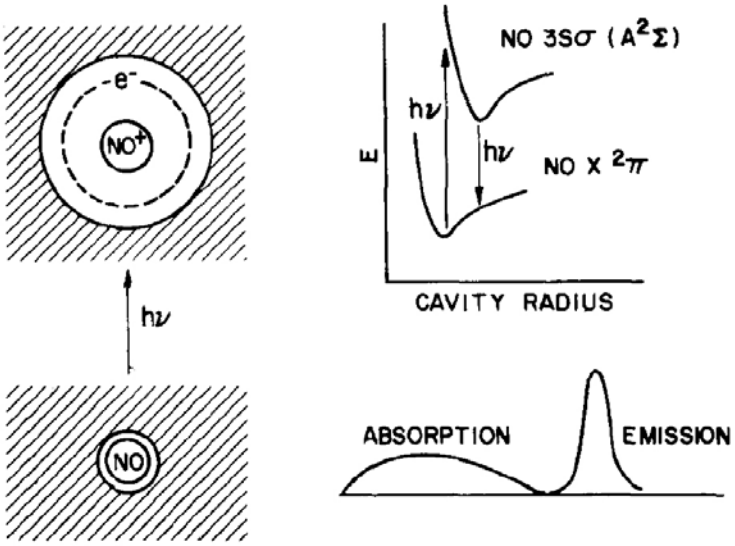

Figure 4-3. Schematic illustration of the mechanism of absorption and emission in the bubble Rydberg model.

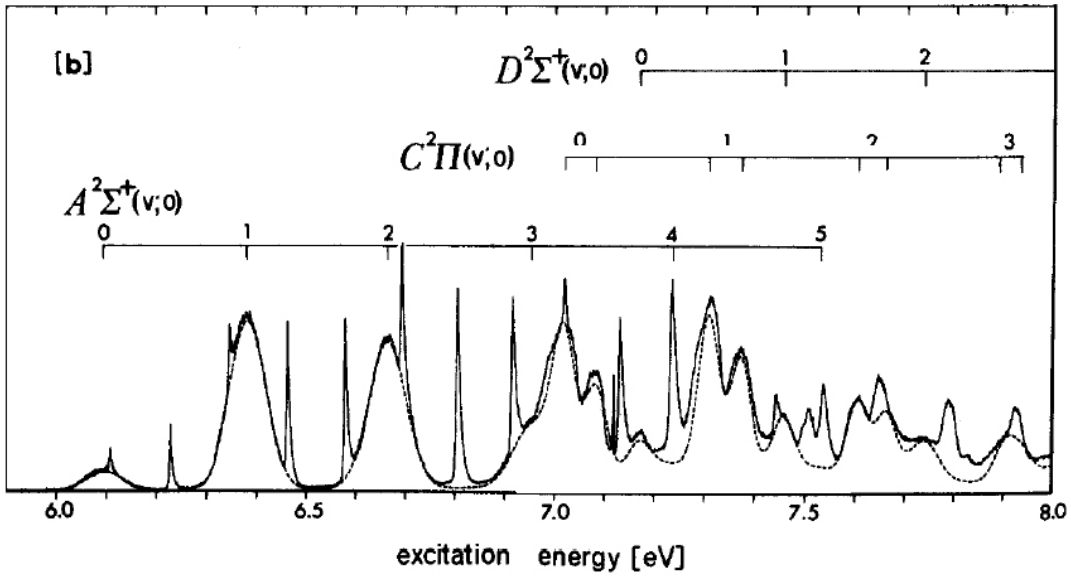

Figure 4-4. Excitation spectrum of global fluorescence of NO in solid krypton.

Considering the fate of the Rygberg state in condensed media closely, one should answer a fundamental question: does this state keep a parentage to the free molecule? In other words, can energy levels be described by perturbed levels of a gas phase molecule.

To answer this question, let us consider the excitation and relaxation of Rydberg states with n = 3 of NO in matrices that are well understood [11, 12]. The main aspects of these processes are shown in Fig. 4-3. First, vertical excitation from the ground state causes a strong overlap of the electron density of the molecule and adjacent atoms. Then, Pauli repulsion leads to the fast initial expansion of the cavity around the excited molecule followed by the oscillatory response of first solvation shell. [12] This cavity relaxation process was found to

release up to 0.5 eV into the host media in the form of phonons. [8, 13] The timescale of about 5 ps [12] is close to the bubble formation time in helium. Consequently, emission (fluorescence) from the excited state occurs from the new cage configuration around the embedded molecule. In this case line positions are close to their gas phase values.

In the excitation spectra of NO in solid krypton (solid line, Fig. 4-4), one can distinguish broad bell-shaped bands and a series of sharp features. The spacing between the broad peaks corresponds to the distance between vibrational levels in the gas-phase NO molecule. Moreover, the widths are approximately the same, and the spectrum in Fig. 4-4 can be fit by using Gaussians peaks (dashed line, Fig. 4-4). Sharp lines belong to the progression $X^2\Pi \rightarrow B^2\Pi$. [8]

Consequently, this spectrum can be simulated using the diatomic constants of a free molecule. Namely, gas phase lines are blue-shifted and broadened. Furthermore, the relative intensities of peaks corresponding to different vibrational states are close to the relative intensities of gas-phase absorption of vibrational bands; therefore, interaction of the Rydberg orbital with $n = 3$ and the host media does not significantly change gas phase Franck-Condon.

Studies of the $A^2\Sigma$ Rydberg state of NO in matrices demonstrated that in all these hosts the absorption bands experience severe broadening (700 – 2000 cm^{-1}) and are blue shifted by 3500-7000 cm^{-1} (See Table 4-2) due to the strong interaction of the extended orbital with the matrix environment [4-6, 8].

Host	Gas-matrix shift / eV	FWHM / eV
Solid H_2	0.6	0.24
Solid D_2	0.73	0.24
Solid Ne	0.8	0.18
Solid Ar	0.6	0.12
Solid Kr	0.62	0.12
Solid Xe	0.32	0.08

Table 4-2. Gas-matrix absorption shifts and linewidth of the lowest Rydberg state $A^2\Sigma$ ($\upsilon = 0$) [4-6, 8, 14]

Whereas a compact ground state is almost unperturbed, diffuse Rydberg orbitals are shifted towards higher energies. Emission lines are much narrower (500-650 cm^{-1}) than absorption lines as shown in Fig 4-3, and line positions are close to their gas phase value. This effect can be explained in terms of efficient relaxation of the cage around Rydberg state. [15]

During the next several nanoseconds after formation of the Rydberg state, the molecule embedded in the matrix can be involved in a relaxation cascade if excitation energy is higher than 50000 cm^{-1}. The Rydberg-valence relaxation is known to occur only from relaxed bubble configuration of the Rydberg state on the timescale of one nanosecond. The strength of Rydberg-valence coupling for two particular states depends strongly upon the media. [8]

However, for Rydberg states with $n > 3$ the overall picture is not so clear. Over 30 years ago Roncin et al. discovered the disappearance of Rydberg spectrum of NO trapped in rare gas matrices, which attracted a lot of interest to this research area. [16] Initially, this observation was attributed to the fact that these states are extremely broadened; they would merge into continuum and disappear from absorption. The Rydberg state with n = 3 and 4 were detected only in neon, in all other rare gas matrices only states with n=3 can be observed despite of numerous attempts to detect the higher members of the Rydberg series.

In neon, the blue shift of Rydberg states with n=4 is even more dramatic (1.2 eV) than for the lowest Rydberg state. [17] Whereas the gas phase vibrational spacing is preserved, the relative intensities distribution does not follow gas phase Franck-Condon factors. Gas-to-matrix shifts and linewidths scale as $s\sigma > p\sigma > p\pi$.

This cut-off of high Rydberg states is not unique to NO. For molecules such as C_2H_2, $C_{10}H_8$, CS_2, H_2O, OSC, D_2, and H_2, only the lowest Rydberg excitations have been observed in rare gas matrices. [17] These excitations can be described as blue-shifted molecular levels. In the molecules C_2H_4, C_6H_6, and CH_3I, high Rydberg excitations were reported and the transition energies can be interpreted in terms of Wannier excitations, which are widely used to describe the electronic absorption in rare gas solids. [18] In this case, the embedded molecule is considered as a bound electron-hole pair, and the parentage to the free molecule is lost. Another way of unified description of Rydberg excitations in matrices is the so called “quantum defect” model. [19] This model supposes that the

"electron – positive center" interaction in the solid is the same as if the species is isolated in the cavity with the defined diameter. The Coulomb potential is screened outside this cavity.

Neither the Wannier model nor the quantum defect model could account for the cut-off of high Rydberg. Chergui et al. [17] suggested that the vertical transition energies of these states lie above the adiabatic ionization limit and could not be observed under employed experimental conditions.

An elegant way to excite high Rydberg states has been found by Zerza et al. [20]; to be exact, the Rydberg-Rydberg transitions were induced in argon matrices by absorption from $A^2\Sigma$ state. Higher Rydberg states, which could not be observed by excitation from the ground state, were probed by the depletion from fluorescence from the $A^2\Sigma$ state.(Fig. 3–5) The Rydberg-Rydberg transitions are red-shifted; for instance, ($n=3 \leftrightarrow n=4$) splitting is shifted by 0.65 eV if compared to gas phase splitting, which suggests a compression of the Rydberg series as well as a red shift of the ionization potential.

The bandwidths of Rydberg-Rydberg bands are on the order of several hundred wavenumbers, which is significantly smaller than the linewidths of the ground state– low Rydberg excitations (that is ≈ 2000 cm^{-1}, see Table 4-2). The continuum absorption structure above 1.8 eV (See Fig 4-5) is attributed to transitions with n > 4 tightly packed in a tiny energy range.

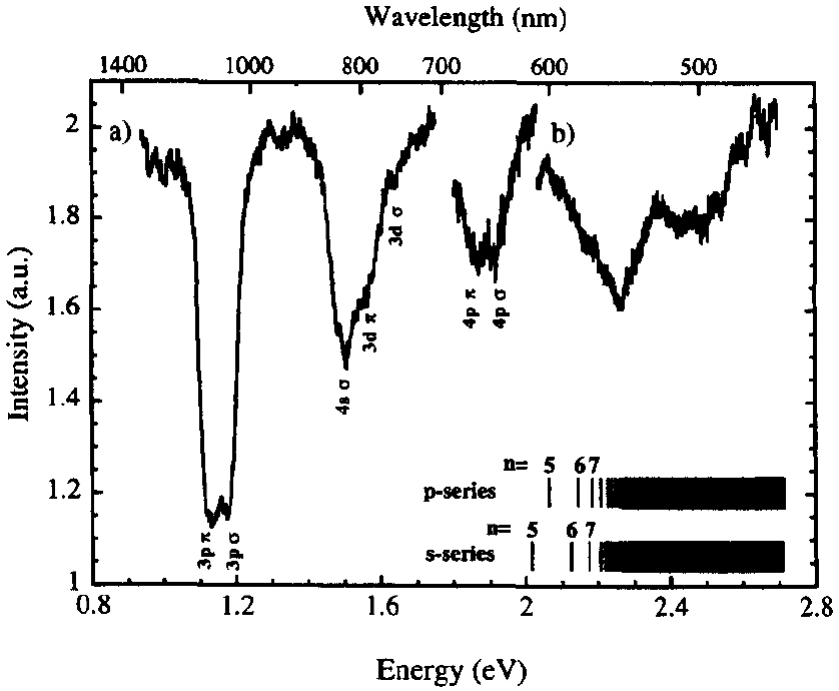

Figure 4-5. Fluorescence signal of the NO $A^2\Sigma$ (0, υ″) emission as a function of probe wavelength. The dips represent depletion of the fluorescence signal due to depopulation of the $A^2\Sigma$ state to higher Rydberg states (Adapted from ref [20])

In conclusion, the energy levels of NO trapped in matrices excited to the lowest Rydberg states (n = 3) can be considered as perturbed levels of their gas phase counterparts. For higher Rydberg states, the formation of extended orbitals can be suppressed, and the parentage to the gas phase molecule can be partially or completely lost.

4.3. NO – rare gas complexes

No experimental spectroscopic data is available on the NO-He complex due to its floppiness. Several present-day theoretical studies of this system

provided different results for the geometry of the ground state of this complex. [21-23] The recent paper by Cybulski et al. suggests that the NO·He complex has T-shape geometry and is bound by ~ 7 cm^{-1}.[22] The value of ε is ~25 cm^{-1} and the distance from the helium atom to the center of mass of NO molecule, r_e ~3.3 Å. A substitution of these values into equation (2.8) proves the localization of NO molecule in the ground state is near the center of the droplet.

Neither experimental, nor theoretical studies of electronically excited NO-He complexes are available at the present time. Wright et al. suggested that the Ã state of the NO·He complex is very weakly bound, and most likely dissociative. [14] This assumption is based on trends in the spectroscopy and bonding of the Ã state of the NO·Rg complexes. Therefore, when the NO molecule is excited into the Rydberg state inside the droplet, the van der Waals interaction between helium and the molecule is weaker than for the ground state. The molecule can be pushed toward the surface or ejected from the droplet due to stronger repulsion of the extended Rydberg orbital. One can predict the formation of a "dimple"-like structure that is similar the structure formed by alkali atoms attached to the surface of the droplet.

In contrast, $C^2\Pi$ and $D^2\Sigma$ states are expected to be bound more strongly than the ground states. But on the other hand, the excluded "volume" of the Rygberg orbital is larger (See Table 4-2) than for the $A^2\Sigma$ state; and according to Ancilotto's formula (2.8), the extraction of the Rydberg state to the surface of the cluster is very likely.

The closed shell $^1\Sigma^+$ cation is much more strongly bound to helium than the neutral molecule. A few *ab initio* studies were devoted to the NO^+·He cationic complex. [23] Wright et al. estimated the NO^+-He pair interaction potential ε to be equal to 198 cm^{-1}; the minimum energy geometry is R_{NO-He}=2.78Å [24], which strongly suggests that the NO^+ ion would be located in the middle of the droplet.

If the Rydberg electron in the NO·Rg complex is excited to extended orbital (n > 4), the question is if this electron localized on the NO moiety or Rydberg orbital is big enough to enclose the $NO·Rg^+$ core. Summarizing the available data on NO·Rg complexes, the interaction NO–Rg increases with the radius of Rydberg orbit, and the properties of NO·Rg are expected to converge to those of respective cations. In other words, the $NO·Rg^+$ "nucleus" surrounded by diffuse electron will be formed, and a similar tendency might be expected for an NO molecule in high Rydberg states embedded in the helium cluster or attached to its surface. Very likely helium atoms will penetrate inside of the Rydberg cloud forming an strongly bound $NO^+·He_m$ core.

4.4. References

1. NIST, *NIST*. 2005, http://webbook.nist.gov/.

2. Miller, J.C. and R.N. Compton, Journal of Chemical Physics. 1986. **84**(2): 675.

3. Shafizadeh, N., P. Brechignac, M. Dyndgaard, J.H. Fillion, D. Gauyacq, B. Levy, J.C. Miller, T. Pino, and M. Raoult, Journal of Chemical Physics. 1998. **108**(22): 9313.

4. Chergui, M. and N. Schwentner, Journal of Chemical Physics. 1989. **91**(10): 5993.

5. Chergui, M. and N. Schwentner, Journal of Chemical Physics. 1992. **97**(5): 2881.

6. Vigliotti, F., M. Chergui, M. Dickgiesser, and N. Schwentner, Faraday Discussions. 1997(108): 139.

7. Vigliotti, F., A. Cavina, C. Bressler, B. Lang, and M. Chergui, Journal of Chemical Physics. 2002. **116**(11): 4542.

8. Chergui, M., R. Schriever, and N. Schwentner, Journal of Chemical Physics. 1988. **89**(12): 7083.

9. Zacharias, H., F. deRougemont, T.F. Heinz, and M.M.T. Loy, Journal of Chemical Physics. 1996. **105**(1): 111.

10. Zacharias, H., J.B. Halpern, and K.H. Welge, Chemical Physics Letters. 1976. **43**(1): 41.

11. Goodman, J. and L.E. Brus, Journal of Chemical Physics. 1977. **67**(3): 933.

12. PortellaOberli, M.T., C. Jeannin, and M. Chergui, Chemical Physics Letters. 1996. **259**(5-6): 475.

13. Ossicini, S., Journal of Physics and Chemistry of Solids. 1985. **46**(1): 123.

14. Barr, J.D., J.M. Dyke, P. Mack, D. Smith, and T.G. Wright, Journal of Electron Spectroscopy. 1998. **97**: 159.

15. Emery, L. and K.S. Song, Journal of Physics C-Solid State Physics. 1986. **19**(14): 2469.

16. Roncin, J.Y., H. Damany, and J. Romand, J. Mol. Spectroscopy. 1967. **22**: 154.

17. Chergui, M., N. Schwentner, and W. Bohmer, Journal of Chemical Physics. 1986. **85**(5): 2472.

18. Schwentner, N., E.E. Koch, and J. Jortner, *Electronic excitations in condensed rare gases*. Vol. 107. 1985: Springer.

19. Resca, L. and R. Resta, Physical Review B. 1979. **19**(4): 1683.

20. Zerza, G., F. Vigliotti, A. Sassara, M. Chergui, and V. Stepanenko, Chemical Physics Letters. 1996. **256**(1-2): 63.

21. Zolotoukhina, T.N. and S. Kotake, Journal of Chemical Physics. 1993. **99**(4): 2855.

22. Klos, J., G. Chalasinski, M.T. Berry, R. Bukowski, and S.M. Cybulski, Journal of Chemical Physics. 2000. **112**(5): 2195.

23. Lee, E.P.F. and T.G. Wright, Journal of Chemical Physics. 1998. **109**(1): 157.

24. Soldan, P., E.P.F. Lee, and T.G. Wright, Journal of Chemical Physics. 2002. **116**(6): 2395.

Chapter 5: Results

5.1. Multiphoton ionization of NO by nanosecond pulses

5.1.1. TOF spectrum

In the experiments described in this Section we observed formation of positive ions upon the excitation of helium droplets doped by NO molecules by laser radiation in the range 22,222–27,816 cm^{-1} that corresponds to the excitation of the low lying vibrational states of the $A^2\Sigma$ state (gray area, Fig. 4–1).

An example of TOF mass spectrum ($h\nu$=24,330 cm^{-1}) is shown in Fig.5-1. The most intense peak corresponds to NO^+ ion (m/Z = 30 amu). The presence of background gaseous NO in the detection region due to diffusive flow of NO from the pickup cell also leads to production of NO^+ when the laser hits the resonance of a free NO molecule. However, we make sure that the intensity of the peak on the spectrum can be attributed to the NO^+ ions originated only from the droplets.

At every wavelength we recorded background TOF spectrum with closed helium droplet beam and then subtracted it from the spectrum with helium droplet beam open. In the region away from free-molecule bands more than 90% of NO^+ ions formed originated from doped helium droplets. The presence of weak non-resonant signal can be explained by ionization of background NO gas.

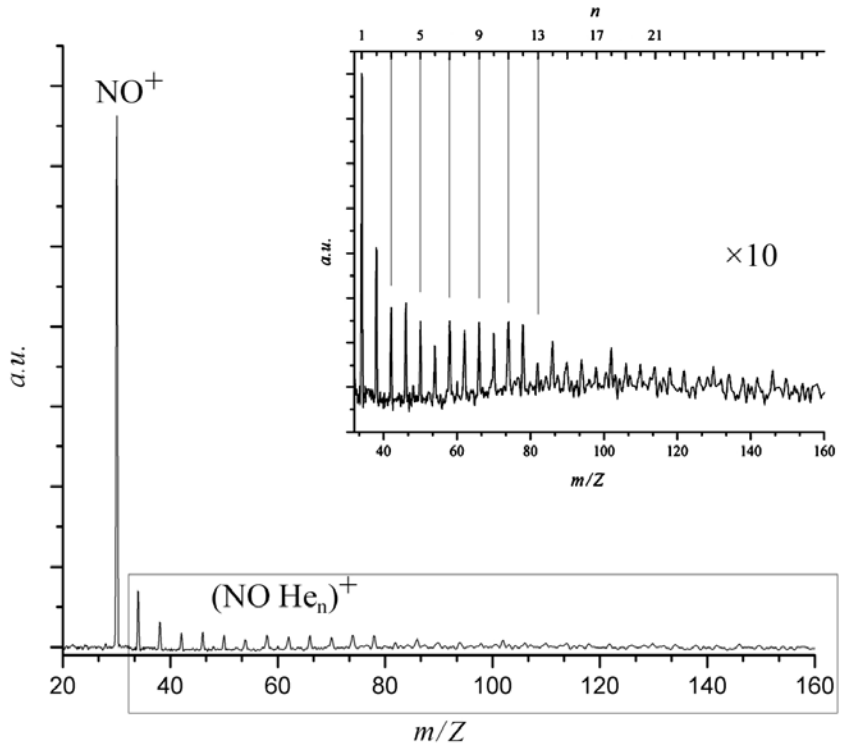

Figure 5–1. Example of TOF mass spectrum of ions formed as the result of multiphoton ionization of NO embedded in helium droplets ($h\nu$ = 24330 cm^{-1}). The most intense peak corresponds to the NO^+ ion (m/Z = 30 amu.). A progression of $(NO{\cdot}He_m)^+$ clusters (m/Z = 34, 38, 42, 46… amu.) is shown at the insert, the signal from $(NO{\cdot}He_m)^+$ fragments is magnified 10 times. Top axis shows the amount of helium atoms attached to NO core.

Beside the NO^+ peak, we observed progression of the peaks at masses 30+4·n amu, n = 1…20. These peaks are absent in the background spectrum. We attributed these peaks to the formation of the $(NO{\cdot}He_m)^+$ complexes, where n is the number of helium atoms attached to NO^+ core. The formation of NO ion with

attached helium is inevitable evidence that NO is located in the vicinity of helium droplet during ionization. The intensity of the peaks gradually goes down with *n* and experiences an abrupt decrease at *n* equal to 12 or 13. We suppose that intensity of the peak correlates with the stability of the $(NO{\cdot}He_m)^+$ complex. It was found that for an atom or a small molecule about twelve helium atoms are required to form first solvation shell, and therefore these complexes are most stable. Section 5–2 discusses possible mechanism of multiphoton ionization.

5.1.2. Wavelength dependence of TOF spectra

In the region 22222 – 27816 cm^{-1}, we recorded TOF spectra with a step equal to 60 cm^{-1}. This region covers several low vibrational levels of the $A^2\Sigma$ state as well as ground vibrational levels of the $C^2\Pi$ and $D^2\,\Sigma$ states as can be seen from Fig. 4–1. Formation of $(NO{\cdot}He_m)^+$ clusters was observed for all energies. After subtraction of background spectrum, intensities of signals at $m/Z = 30+4{\cdot}n$ amu, $n = 0\ldots9$ (monitoring $(NO{\cdot}He_m)^+$ ions) were integrated for all TOF spectra. These spectra in the range 23250 – 27816 cm^{-1} are shown in Fig 5–2. The number on the top of the graph represents the amount of attached helium atom. Comparison of the spectra corresponded to different ionic complexes $(NO{\cdot}He_m)^+$ shows that all these spectra look alike; and there is no fundamental difference between them.

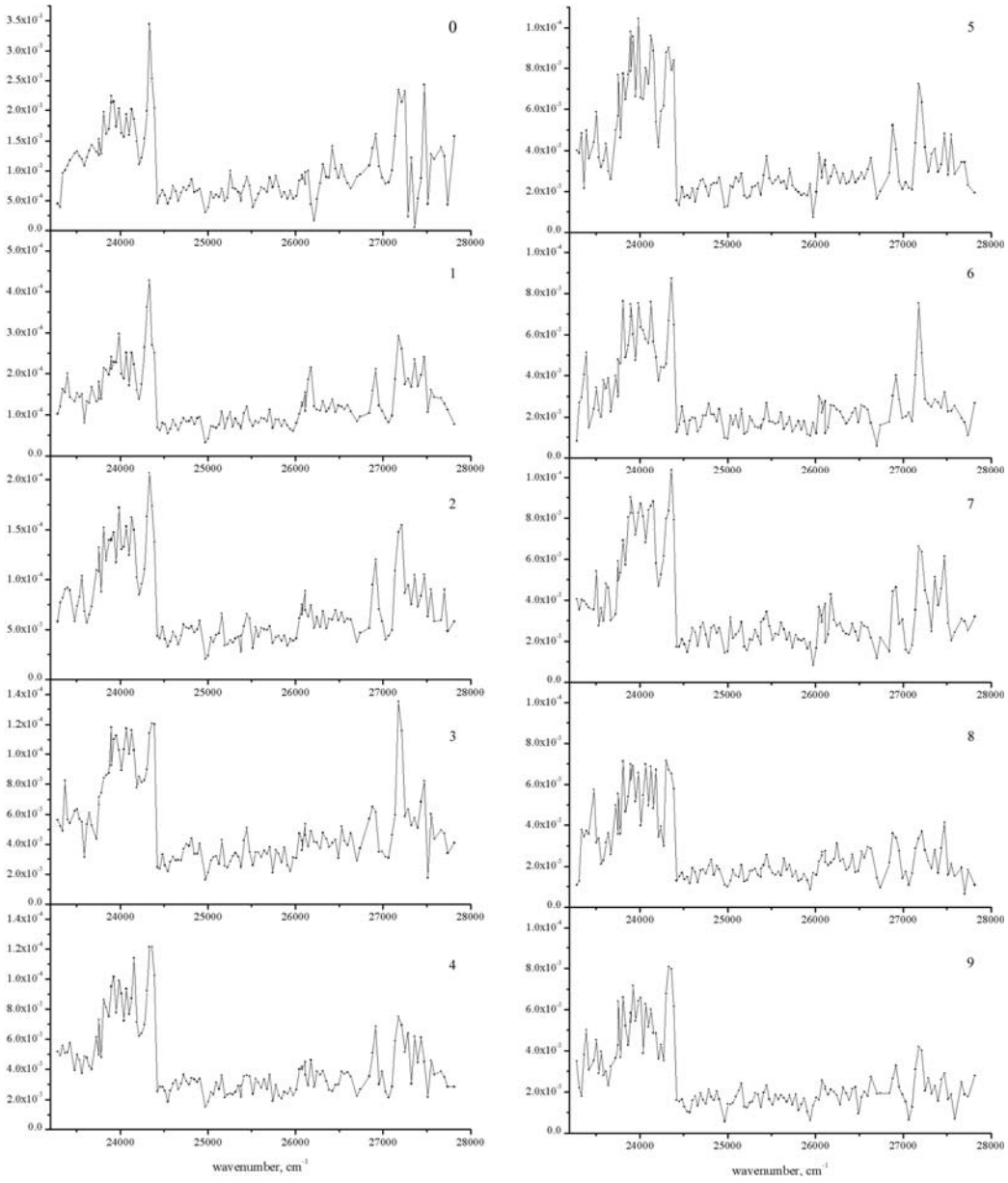

Figure 5–2. Mass selected MPI spectrum of NO molecule in helium droplets. The intensities of the signal from $(NO{\cdot}He_m)^+$ ions at $m/Z = 30+4{\cdot}n$ amu, $n = 0\ldots9$ were integrated for all TOF spectra in the range 23250 – 27816 cm^{-1}.

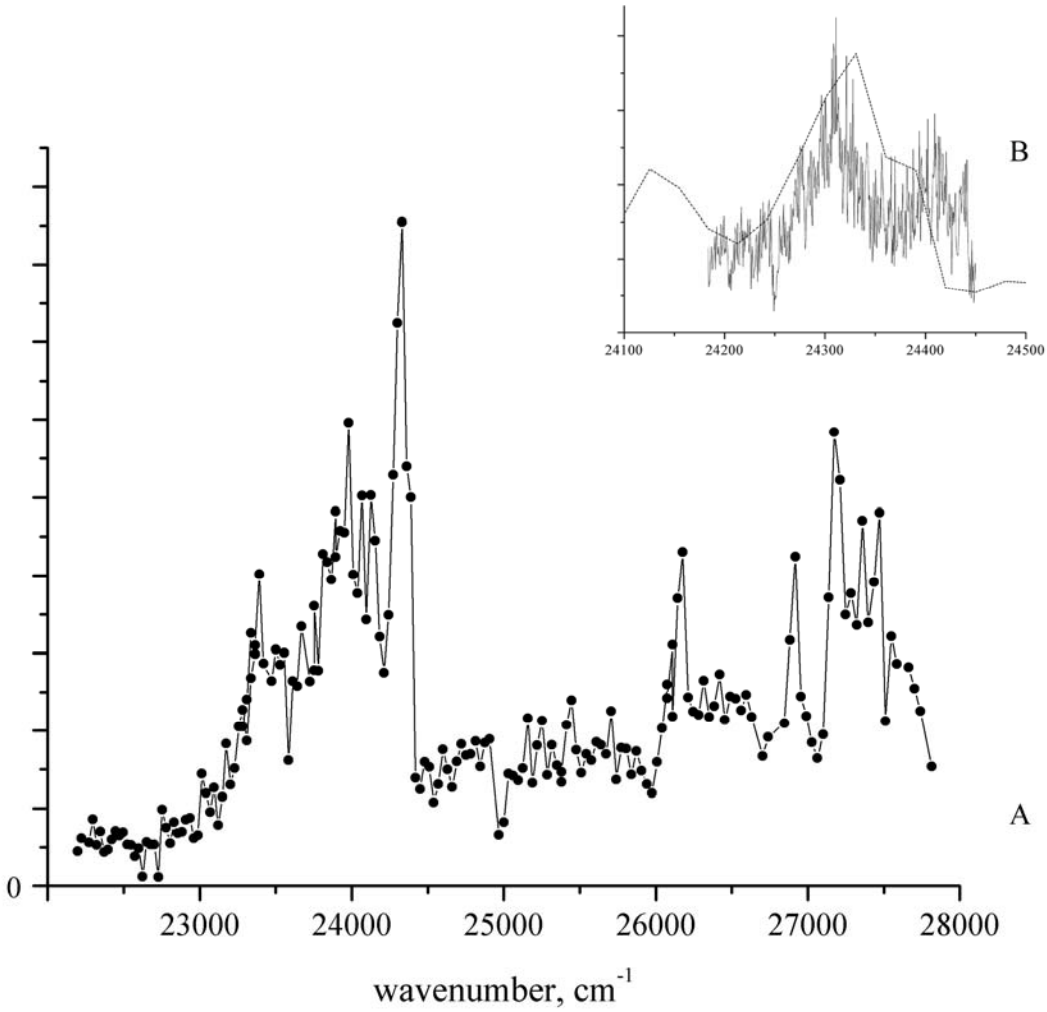

Figure 5–3. Mass selected MPI spectrum of the NO molecule in helium droplets. Formation of $(NO{\cdot}He)^+$ was monitored. A –Signal at mass 34 integrated for TOF traces recorded for every 60 cm^{-1} in the region 22,222-27,816 cm^{-1}. B – The ion signal at amu 34 recorded directly in the region 24,185-24,445 cm^{-1} with resolution 1 cm^{-1} and 10000 averaging. (solid line) The spectrum low-resolution spectrum, which is shown in Fig. A in the same region (doted line).

When $h\nu < 23{,}250$ cm^{-1}, $(NO{\cdot}He_m)^+$ the signal is weak and reliable calculation of intensities of with $n>1$ is not possible; only intensity of the signal from NO^+ and $(NO{\cdot}He)^+$ ions have been analyzed in the 22,222–23,250 cm^{-1} region. The wavelength dependence of signal at m/Z=34 amu is shown in Fig 4–3 A in the full spectral range 22,222–27,816 cm^{-1}. This spectrum has the best S/N ratio and cannot be distorted due to incomplete subtraction of background signal. Thus, we will use it for further analysis.

Several channels lead to formation of NO^+ ions upon excitation of NO molecule embedded in the helium droplet:

1. NO molecule attached to the helium cluster is ionized.
2. Excited NO molecule is ejected from the droplet and ionized in gas phase
3. NO^+ is a product of $(NO{\cdot}He_n)^+$ dissociation.

The similarity of wavelength dependence of production of NO^+ and $(NO{\cdot}He_n)^+$ ions leads us to conclusion that all these ions are formed by the same mechanism close to the droplet surface or within the droplet.

Unlike the excitation spectrum of NO molecule confined in rare gas matrices, the spectrum we recorded cannot be easily rationalized in terms of overlapping of broadened and shifted vibrational bands of NO molecule (Section 4 – 2, Figure 4–4). We observed the ionization onset close to the position of the $A^2\Sigma$ ($\nu' = 0$)←$X^2\Pi$ ($\nu'' = 0$) gas phase transition. ($h\nu$=22,138 cm^{-1}) The ionization signal

grows fast with the increase of photon energy; then it decreases abruptly around 24500 cm^{-1}.

The spectrum contains two broad asymmetric features at ~ 24,250 cm^{-1} and 28,000 cm^{-1}. These features can be observed for all $(NO{\cdot}He_m)^+$ ions. The most intense signal is observed around $h\nu$ = 24,250 cm^{-1}. The high resolution spectrum of $(NO{\cdot}He)^+$ intensity was recorded in the region 24,185 – 24,445 cm^{-1} (Fig. 5–3B). No addition fine structure was found. The peak around $h\nu$ = 26,250 cm^{-1} is due to noise because it can be seen only at several masses. (Fig 5–3A) Possible explanation of observed spectral dependence of ionization of NO molecule embedded in the helium droplet will be given below in section 5-4.

5.2. Discussion of ionization mechanism

5.2.1. General mechanism of multiphoton ionization

Mechanism of multiphoton ionization of a free NO molecule is well known. [1] It follows the excitation scheme shown in Fig. 5-4. At first, two–photon excitation promotes the NO molecule into the low Rydberg state. Then, the molecule is ionized by one or two photons. The ionization step is usually saturated. It is nontrivial that NO molecules embedded in helium droplets are ionized via two-photon resonances that access the low-lying Rydberg intermediate states, as indicated in Fig. 5-5. It is reasonable to divide the ionization process into three independent steps (Figure 5-5).

The first step is two-photon excitation of the system from its ground state, in which the embedded NO interacts weakly with the surrounding helium, to one or more low-lying Rydberg states creates a state that has a significant amount of nuclear potential energy. Namely, in this vertical transition, the surrounding helium lies in close proximity to the excited NO, with the excited electron extending into the helium. This results in a blue shift and broadening due to the overlap of the electron densities of the helium atoms and the Rydberg electron. It is important to emphasize that this step takes place close to the center of the droplet; therefore, the finite size effects should be minor or negligible.

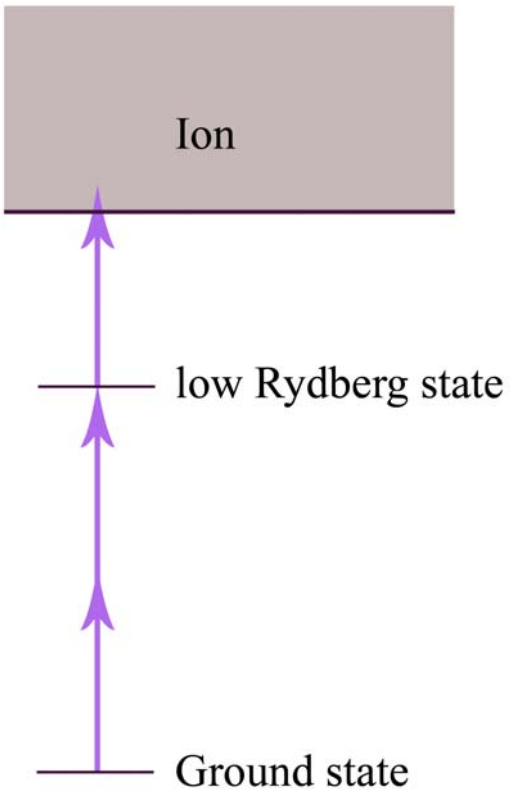

Figure 5-4. Ionization scheme of the NO molecule in gas phase.

Thus, helium will be repelled and it will move away to create a bubble–like state (denoted as NO* below). On the basis of the calculations of Groß and

Spiegelmann, it is expected that the diameter of this NO* Rydberg bubble is 8-9 Å. [2] Bubble formation occurs on a timescale of several picoseconds and results in the release of energy by phonon excitation into droplet. This energy dissipated by evaporation of helium atoms until, given enough time, the low temperature superfluid environment is recovered. [3]

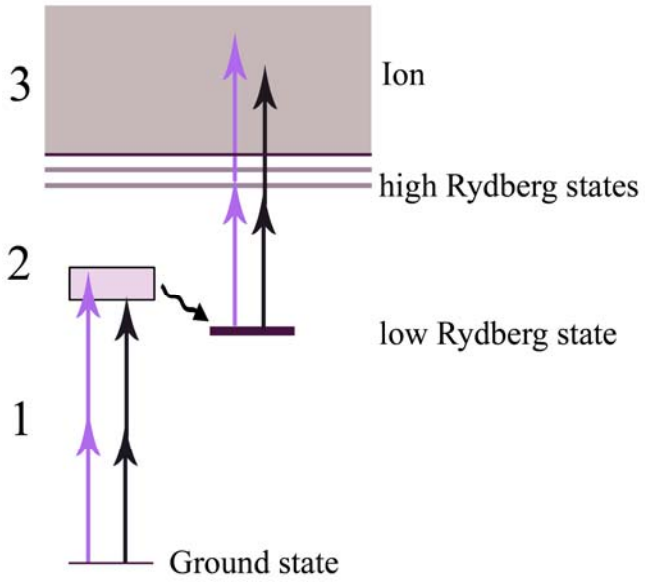

Figure 5-5. Scheme of multiphoton ionization of the NO molecule in helium droplets. Step 1 – Vertical electronic excitation of the NO molecule from the ground state to the low Rydberg state. Step 2 – Motion of the Rydberg bubble toward the surface of the helium cluster. Step 3 – immediate ionization and formation of $(NO{\cdot}He_m)^+$ clusters.

The next step (Step 2, Fig. 5–5) includes relaxation of the Rydberg bubble with respect to the surface of the droplet. Extremely weak binding of NO·He complex strongly suggests that a Rydberg bubble formed deep within the droplet

will move to the surface, where it can remain, being bound to the surface. The properties of the Rydberg bubbles are discussed in the Section 5.2.2.

Later, the third step, immediate ionization and formation of "snowballs", takes place near the droplet surface. This step may proceed via two-photon non-resonant process as well as it may involve an accidental resonance of the energy of the third photon with the higher Rydberg levels of the NO molecule. If one consider the system NO^+ -helium, it is clear that the energy minimum of this system corresponds to the location of the ion in the center of the droplet. Therefore, the escape of the cluster, which size is much smaller than the size of helium droplet, can be explained only in terms of non-equilibrium dynamics.

5.2.2. Surface bound NO* Rydberg bubble

Let us now consider the most likely scenario, in which a NO* bubble reaches the droplet surface, where it remains, residing at a dimple in the surface. The fact that the Rydberg bubble is bound to surface during the ionization is confirmed by our experimental observations. If NO^* leaved the droplet before the ionization we would observed only NO^+ as a result of ionization sequence that is not the case.

Furthermore, Rydberg states are predicted to be bound to the surface of liquid helium. [4] The wave functions of electron can be "semi-spherical" if the interaction of the electron with ionic core exceeds the electron interaction with its image. In the opposite case, the "flat" state is formed. The NO* is bathed in intense electromagnetic radiation of a laser pulse, and it is suggested that

photoionization is dominated by contributions from the NO* that resides on the surface for two reasons: (i) the NO* spends most of its time on the surface; (ii) it is easier to eject an electron from NO* into vacuum than into helium. It is assumed that the excitation rate brought about by the intense radiation field is not so large that a significant percentage of NO* is photoionized as it makes its way to the surface.

The nature of the force driving the molecule toward the surface is an open question. At first, NO molecule cannot be localized in the vicinity of the center of the droplet without giving it enough momentum to ensure transport to the surface. This is a direct consequence of the uncertainty relation $\Delta p \, \Delta x \geq 1 / 2$. Moreover, the energy of the system is lower with NO* at the surface than with NO* embedded in the helium, providing an additional driving force for NO* going to surface. An addition contribution to driving force comes from instability of the bubble close to the surface (Section 2.2.2.). Once a molecular bubble reaches the helium droplet surface, spontaneous destruction of the bubble occurs. The surface energy accumulated in the free surface of the molecular – helium interface is released and dissipated by the droplet, and the molecule stays attached to the helium droplet in a dimple as an alkali atom. This surface state does not require formation of large area of helium free surface.

The fact that NO* resides at the surface facilitates its photoionization. This transport process occurs concomitantly with vibrational relaxation of the NO* moiety, in the event that the NO^+ is formed with vibrational excitation. The wave

function of the excited electron of surface-bound NO* is expected to lie, for the most part, outside the droplet, as this minimizes the energy.

If the NO* momentum is large (*e.g.*, as when it derives from an $(NO)_x$ cluster that dissociates following photoexcitation, yielding NO* + $(NO)_{x-1}$), it will undergo inelastic collisions with the helium and lower its velocity. This statement has been confirmed by experiments of Drabbels *et.al*. [5] They found efficient (80%-90%) dissipation of translation energy of recoiled fragments formed after CH_3I and CF_3I photodissociation. However, even a slowly moving particle in a superfluid droplet will undergo photoionization most often at the surface. For example, at 40 $m\ s^{-1}$, a particle travels 100 Å in 250 ps, which is much less than both the laser pulse duration (~ 10 ns) and the spontaneous emission lifetime.

5.2.3. Liberation of $(NO{\cdot}He_m)^+$ clusters

In this section we propose possible mechanism of liberation of the snowballs that is shown in Fig 4-6. NO^* absorbs one or two photons close to the surface of the droplet. The subsequent ejection of an electron from NO* into vacuum creates an NO^+ moiety at the edge of the droplet. Helium is attracted strongly to this ion, ensuring vigorous dynamics in which a helium snowball is formed around the NO^+, as concomitant evaporation cools and stabilizes the snowball, yielding small positive ions of the form $(NO{\cdot}He_m)^+$. Afterward, the snowball detaches from helium droplet and is accelerated by electric field toward the MCP detector. Unfortunately, it is difficult to provide the quantitative description of this process.

Macroscopic thermodynamic of the liquid helium changes rapidly with the temperature and it is impossible to use it even for a rough estimate. Classical molecular dynamic simulation would have little or no value due to quantum character of helium.

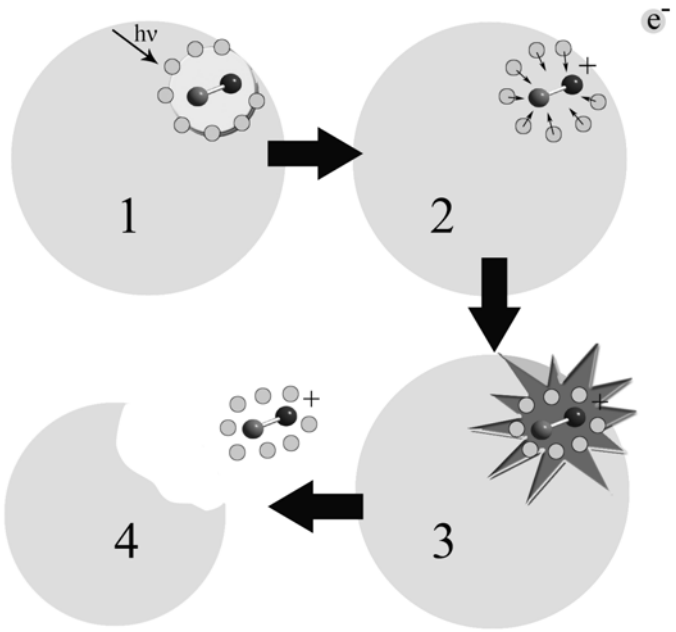

Figure 5–6. Schematic diagram of the mechanism of snowball liberation

Photoionization of the embedded (*i.e.*, completely submerged) Rydberg state is encumbered because it yields an electron in helium, which has its lowest energy with a large bubble, requiring ~ 1 eV for its formation from the compressed initial state in the bulk helium. [6] For helium clusters this value is predicted to be even higher, ~1.35 eV. [7] This precludes the possibility of three-photon ionization in the work reported here, because the photons employed have insufficient energy to

provide ~1–1.5 eV more than for the gas phase counterpart. Even with the NO* bubble located *within* the helium droplet (*i.e.*, before it reaches the surface), it is still possible to detach its Rydberg electron through the absorption of two photons. Were this to happen, however, the electron would find itself in helium, scattering from it and dissipating its nascent kinetic energy. It can either escape into vacuum or remain in the helium, in which case it will form a new bubble in several ps. In turn, this bubble would either: (i) recombine with the NO^+ snowball that is created subsequent to photoionization; or (ii) overcome the Coulomb attraction to the NO^+ snowball and escape into vacuum.

In the case (i), the resulting excited state(s) will be de-excited through interaction with the helium and / or spontaneous emission. The amount of available energy (*i.e.*, essentially the NO ionization potential) is so large that it can result in the evaporation of nearly all of the helium in droplets with $n \sim 10^4$. If, on the other hand [case (ii)], the electron bubble escapes into vacuum before evaporating, it is expected to be cold, because it will have relaxed to its lowest bubble state. As has been mentioned above, Neumark and coworkers, in examining the photoionization of undoped helium droplets, [8] report that the resulting electrons have almost zero velocity. The formation of such slow electrons is consistent with their nascent kinetic energies having been efficiently dissipated within the helium droplet before they escape into vacuum. Were an NO^+ ion created (say, at $t = 0$) deep within its helium cluster, with the corresponding electron ejected from the cluster into vacuum, it is improbable that

small clusters such as the ones presented in Fig. 5–1 would be produced. Phonons are created by the abrupt introduction, at $t = 0$, of a highly non-equilibrium situation.

Namely, the NO* bubble precursor is of such a nature that the helium lies outside the volume occupied by its Rydberg electron. This is the situation at $t < 0$. Then, at $t = 0$, the NO^+ is created, which draws helium toward itself, with NO^+–He binding energies of ~ 200 cm^{-1} per helium atom for the first solvation shell. This heats the inside of the cluster and evaporation is inevitable. However, the amount of energy spent in evaporation is relatively small compared to that due to electronic excitation. Thus, it is expected that large clusters will be produced.

We see no evidence of such large clusters being formed. Referring to Fig. 4-1, the ion signal diminishes almost monotonically as the number of attached helium atoms increases, with the total number of clusters that have ten or fewer helium atoms accounting for ~90% of the ion signal. A caveat that we have not yet been able to address experimentally is the fact that ion signals from large clusters would be spread out over broad mass range that made detection of this signal problematic.

5.2.4. Vibrational relaxation of NO^*.

Several vibrational levels of NO in the $A^2\Sigma^+$ state are accessible by two-photon excitation for 22,222-27,816 cm^{-1}. The vibrational quantum of the $A^2\Sigma^+$ state is 2374cm^{-1} [9], which is sufficient to evaporate ~11 helium atoms from the

first solvation shell as can be estimated from NO^+–He binding energy. Therefore, one would expect the number of the helium atoms in the snowball to decrease when $v' \geq 1$ vibrational state is excited if NO preserves vibrational excitation after the snowball formation. As it can be seen from comparison of the spectra shown in Fig. 5–2, this is not the case. The distribution of the number of helium atoms carried by NO^+ ion does not depend upon the photon energy in this energy range. To the extent that a NO^+ ion formed by ionization of NO^* molecule preserves its vibrational excitation, our experimental results prove that NO^+ core undergoes efficient vibrational relaxation before the snowball is formed. A neutral NO^* can undergo vibrational relaxation, as well as the relaxation of an ion can occur just after the ionization during the snowball formation.

5.3. Discussion of wavelength dependence

The shape of the spectrum presented in Fig. 5-3 is determined by net effect, involving overall absorption of 3-4 photons, with contributions from: (i) a broad range of cluster sizes; (ii) a distribution of NO locations within the cluster for each cluster size; (iii) different NO* vibrational levels; (iv) photoionization of NO* from different locations in the droplet and at its surface; and (v) different mechanisms of ionization.

When the initial two-photon excitation that creates NO* is followed by transport to the surface, a surface state is prepared. As far as the duration of the laser pulse is much longer than the characteristic timescale of surface state

formation, photoionization of NO^* can be treated separately from the two-photon preparation of NO*, *i.e.*, there are no coherences between two-photon NO* production and subsequent NO* photoionization. In this case, the spectrum presented in Fig. 5-3 is the product of two spectra: two-photon excitation and subsequent photoionization. It is essential to learn the foremost step that determines the shape of the spectrum.

The two-photon production of the gas phase NO ($A^2\Sigma^+$, v' = 0) occurs at a photon energy higher than 22,102 cm^{-1} [10], and it is safe to assume that the corresponding spectrum for the production of NO* in helium is blue shifted and broadened, because these effects are well understood and have been observed in a number of inert matrices. Thus, on the basis of analogy with the results obtained by using inert matrices, [11] it is assumed that a two-photon absorption spectrum can be simulated by broad Gaussians.

In general, a probability of non-resonant ionization does not depend strongly upon the photon energy. Recent experiments by Stace et al. [12] demonstrated that the shift between spectral lines corresponding to the same transitions in benzene molecules trapped in helium nanodroplets monitored by the depletion technique and two-photon ionization is less than 1 cm^{-1}.

Referring to Fig. 5-3 and the discussion surrounding it in the previous section, it then remains to explain the features that are robust, *i.e.*, can be verified in all of the entries in Fig. 5-2 and high resolution experiments. Spacings are inconsistent with vibration, and r rotation is out of the question. For example, what gives rise

to peaks that are separated by ~ 500 cm^{-1} for 23,000-24,500 cm^{-1}?

It is most probable that these features are due to higher Rydberg levels that are accessed with one photon from the lowest NO* level. Ionization is then achieved by photoionizing a high Rydberg state. Enhancement of the efficiency of ionization of low Rydberg states of a NO due an accidental resonance with high Rydberg states has been observed in gas phase. In addition, electronic transitions between electronic states are believed to take place close to the surface of the droplet that increases a probability of ionization. Moreover, essentially smaller values of line widths for Rydberg -Rydberg transitions are expected than for ground-Rydberg excitations. [13]

The exact assignment of the observed resonances is complicated due to uncertainty of the amount of heat released by evaporation. Formation of the surface-bound Rydberg state as a next step causes further energy dissipation. The energy of this surface-bound state only slightly deviates from the level gas phase molecule; this shift can be either positive or negative.

For this reason, it is highly probable that the resonance condition for excitation for Rydberg-Rydberg transition is determined only by the energy of the third photon and not correlated to the energy of the first two photons. Within the limits of this assumption, rough estimate gives $n = 4…5$ for the principle quantum numbers for these Rydberg state.

For these states, the Rydberg radius is large enough to accommodate a shell of helium atoms. Thus, it is possible that higher Rydberg levels can be prepared in

which the ($NO \cdot He_m$) ionic core is 0.37 K. In this case, this structure should be extremely stable if *m* helium atoms form complete solvation shell. If one presumes that the probability of escape from the droplet is the same for surface-bound NO^* and ($NO \cdot He_m$) clusters, strong enhancement of signal from $(NO \cdot He_m)^+$ ions with respect to NO^+ and smaller clusters must be observed on TOF spectra in this energy range. This hypothesis contradicts with our experimental results.

On the other hand, if such ($NO \cdot He_m$) ionic core is formed, most of the energy required for liberation of "snowball" would dissipate before the ionization step that lessens prospect of snowball escape. Besides, it is plausible that this ionic core would be bound to helium droplet stronger than NO in Rydberg state with tight orbital and might be submerged.

Consequently, one can assume that the ionization of such species will be hindered and results in the formation of the ionic cluster containing the substantial number of helium atoms that we are not sensitive to. Such effect can be responsible for abrupt decrease of the ionization signal at 23,300 cm^{-1}. If the mechanism proposed above is valid, it should be no strong dependence of the peak position upon the size of initial helium droplet. Likewise, the initial distribution of cluster sizes should not contribute into line broadening.

It is noteworthy that if $n \geq 9$, the diameter of the Rydberg orbital is equal or larger than the diameter of the droplet. It is expected that the ion core will "sink" into the droplet, while the Rydberg electron is located outside the droplet. The negative affinity of electron to helium prohibits electron density from penetration

inside the droplet. Formation of such “large neutral excimer” has been predicted but has not yet been observed experimentally [14], and NO molecule is a promising system for experimental examination of this exotic cluster.

5.4. Future experimental work

It is undoubtedly that we are still far from complete understanding of physics of multiphoton ionization of in helium droplets, and our research group is planning to continue studies in this direction. In this section we present some preliminary data on ionization of NO by two photons as well as by picosecond laser pulses of high intensity. Several experiments are proposed to extend our knowledge of intermediate steps of ionization, and a prospect to apply MPI technique to studies of photodissociation of molecules and molecular clusters in superfluid helium environment is analyzed.

To clarify the influence of the intermediate excitation of the high Rydberg states, we are planning to interrogate the ionization of NO molecule embedded in helium droplets by means of a two-photon ionization spectroscopy. A scheme of this process is shown in Fig. 5-8. In this case, direct ionization of low Rydberg state is indisputable, no accident resonance with high Rydberg levels is possible and recorded spectrum will reproduce the absorption spectrum of NO.

A set of TOF spectra in the range 45,000-48,500 cm^{-1} was recorded, and an example of the TOF spectrum is given in Fig 5-9 (the background signal from gas phase NO has been subtracted). The most apparent difference between TOF spectra obtained by two and multi-photon ionization is that in the case of two-photon ionization the main product is bare NO^+ ion; in addition, the absolute intensity of the signal (number of ion counts) is significantly lower. There are several possible explanations of this phenomenon. First, the density of laser radiation is lower by three orders of magnitude if compared to the experiments described in Sections 5.1 - 5-3, and ionization pattern is different. There is always a distribution of locations of NO within the cluster for each cluster size. The cross section of ionization as well as the structure of snowball is the function of position of the molecule. For this reason, the density of radiation can play an important role in dynamics of ionization. Only molecules with the highest ionization cross section contribute to

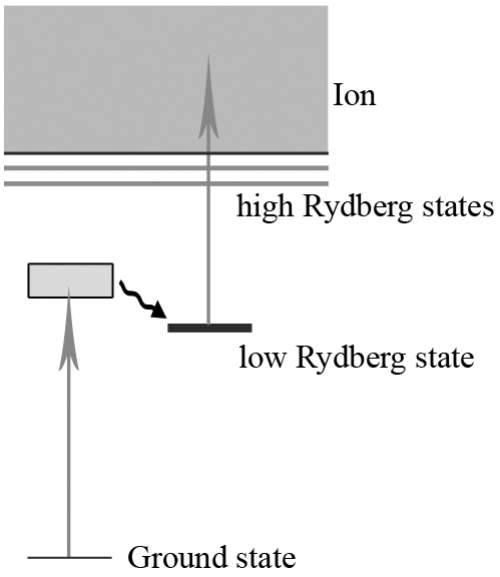

Figure 5-7. Two-photon ionization scheme.

the ion formation. It is plausible that the closer the molecule to the surface the higher the ionization probability and the lower is the probability of snowball formation.

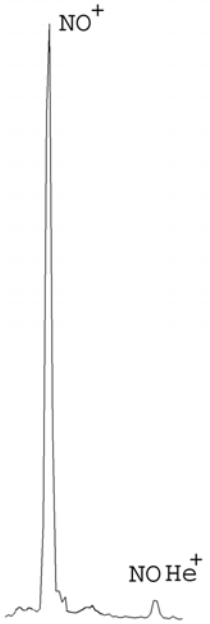

Figure 5–8 Example of TOF mass spectrum of ions formed as the result of two-photon ionization of the NO molecule embedded in helium droplets ($h\nu$ = 47000 cm^{-1}).

Anyways, the first step of ionization, the excitation of the molecule from the ground state to the low Rydberg state should not be affected. It would be extremely informative to scan the region where the intense resonant structure were detected by multiphoton ionization (Fig. 5-3 B). The absence of this structure would strongly suggest the legitimacy of supposition introduced in section 4-4. In addition, if Gaussian-like structure is revealed in this experiment

that would give us an opportunity to calculate the matrix shift for Rydberg excitations in liquid helium droplets.

Due to limitations of our cryogenic setup, we could not change an average cluster size N in a broad range, the maximum accessible droplet size is ~ 15,000 helium atoms. Within $\bar{N}$ = 1,000-15,000, we did not observe any noteworthy dependence of TOF spectra upon $\bar{N}$. For the purpose of elucidation of the role of surface bound Rydberg states in ionization sequence, it would be appealing to investigate the evolution of TOF spectra for $\bar{N}$ =10^3 -10^6. For large clusters the recombination probability for molecules ionized deep below the surface should be close to unity, and only surface-bound species would contribute in TOF spectrum.

Additionally, an average travel distance of the molecule from the center to the surface of the cluster depends linearly upon the radius of the droplet. Dynamics of formation of the surface bound Rydberg state is believed to proceed in subnanosecond region and can be monitored in time-resolved studies.

Making a first step in this direction, we demonstrated that it is possible to ionize the NO molecule and $(NO)_k$ clusters by third harmonic of Nd:YAG laser. The TOF spectrum, which is shown in Fig. 5-10 evinces that very efficient formation of large $(NO{\cdot}He_m)^+$ snowballs with $n \leq 100$. Contrary to the experiments with lower photon density, formation of NO^+ is less favorable than creation of $(NO{\cdot}He_m)^+$ clusters, and it seems like ionization is possible regardless the location of impurity within the droplet.

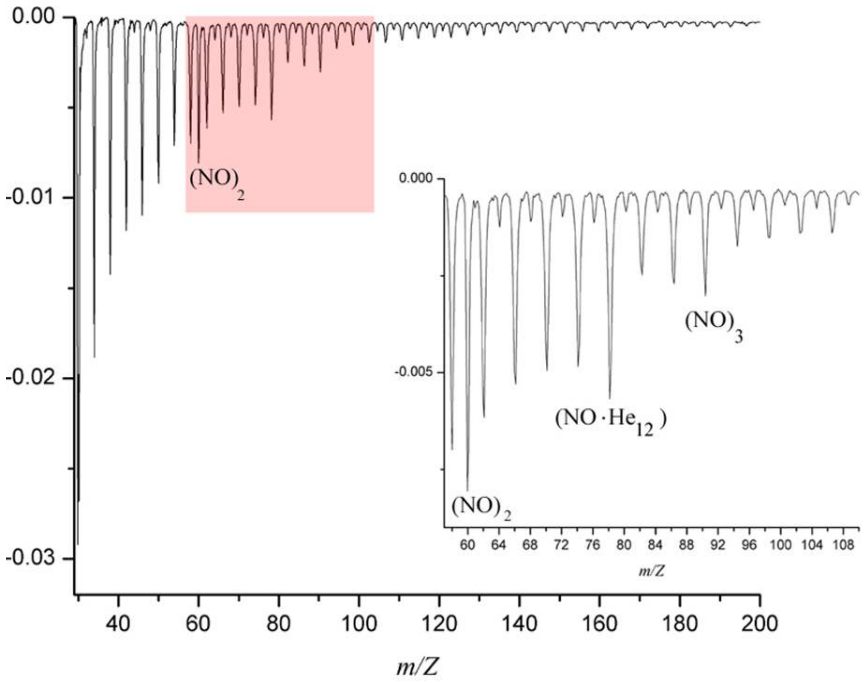

Figure 5-9. Example of TOF mass spectrum of ions formed as the result of multiphoton ionization of NO clusters embedded in a helium droplet ($h\nu$ = 28169 cm^{-1}, τ = 30 ps, E=100 mJ/pulse) There are 2.5 NO molecules pre droplet in average.

Furthermore, MPI technique can be employed to detection of the NO molecule if it is formed as a result of the photoinitiated reaction. In our previous work, we investigated photoexcitation of NO_2 in helium droplets above the gas phase dissociation threshold [15].

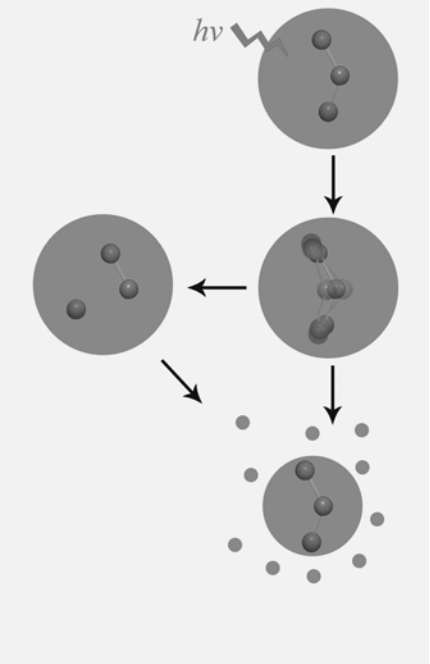

Figure 5-10. Schematic diagram of photoexcitation of NO_2 in helium droplets above the gas phase dissociation threshold

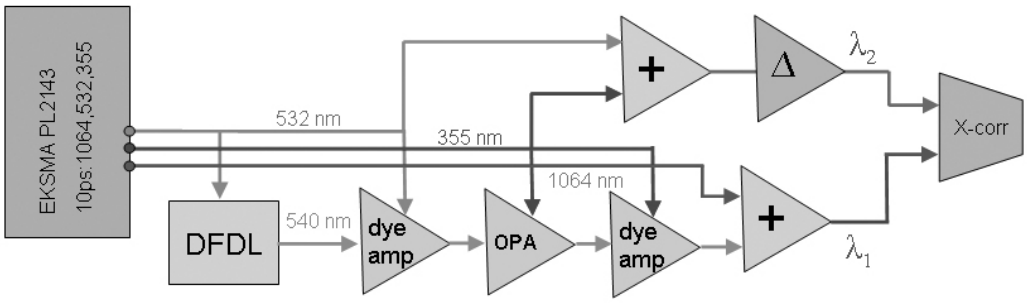

Figure 5-11. Schematic drawing of laser arrangement for proposed picosecond pump-probe experiment

$$NO_2 \xrightarrow{h\upsilon} NO(X^2\Pi) + O$$

Above the gas phase dissociation threshold (D_0 = 25,128.5 cm^{-1} [16]), it shown that there is no *net* unimolecular decomposition up to D_0 + 4300 cm^{-1}.The experiments do not provide direct information about the intra-cluster dynamics of photoexcited NO_2 interacting with its environment. NO_2 may either dissociate and then recombine or get deactivated before dissociation as it shown in Fig. 5-10.

However, these experiments show undoubtedly that fragments do not, to any significant extent, leave the helium clusters and pass into the gas phase. Implementation of MPI detection of NO fragment can help to answer question if the NO_2 dissociates in superfluid helium environment. A layout for pump-probe picosecond experiment is proposed in Fig. 5-12. As a pump, it is rational to use λ_1=365-400 nm to cover substantial range over D_0. The probe wavelength should be chosen so that the NO is efficiently ionized while contribution from multiphoton NO_2 is negligible. From this prospect, the region just below D_0 looks promising.

5.5. References

1. Ebata, T., Y. Anezaki, M. Fujii, N. Mikami, and M. Ito, Journal of Physical Chemistry. 1983. **87**(24): 4773.

2. Gross, M. and F. Spiegelmann, European Physical Journal D. 1998. **4**(2): 219.

3. Stienkemeier, F. and A.F. Vilesov, Journal of Chemical Physics. 2001. **115**(22): 10119.

4. Lerner, P.B. and I.M. Sokolov, Z Phys D Atom Mol Cl. 1989. **14**(2): 173.

5. Drabbels, M. and A. Braun. *Imaging the translational motion of photofragments in liquid helium droplets*. in *228th ACS National Meeting*. 2004. Philadelphia, PA.

6. Buchenau, H., J.P. Toennies, and J.A. Northby, Journal of Chemical Physics. 1991. **95**(11): 8134.

7. von Haeften, K., T. Laarmann, H. Wabnitz, and T. Moller, J Phys B-at Mol Opt. 2005. **38**(2): S373.

8. Peterka, D.S., A. Lindinger, L. Poisson, M. Ahmed, and D.M. Neumark, Physical Review Letters. 2003. **91**(4).

9. Schmid, R., Z. Phys., 1928. **49**: 428.

10. Zacharias, H., F. deRougemont, T.F. Heinz, and M.M.T. Loy, Journal of Chemical Physics. 1996. **105**(1): 111.

11. Vigliotti, F., A. Cavina, C. Bressler, B. Lang, and M. Chergui, Journal of Chemical Physics. 2002. **116**(11): 4542.

12. Curtis, S., A. Boatwright, R.R. Wright, and A.J. Stace, Chem Phys Lett. 2005. **401**(1-3): 254.

13. Miller, J.C. and R.N. Compton, Journal of Chemical Physics. 1986. **84**(2): 675.

14. Golov, A. and S. Sekatskii, Zeitschrift Fur Physik D-Atoms Molecules and Clusters. 1993. **27**(4): 349.

15. Stolyarov, D., E. Polyakova, and C. Wittig, J Phys Chem A. 2004. **108**(45): 9841.

16. Jost, R., J. Nygard, A. Pasinski, and A. Delon, Phys. Rev. Lett. 1997. **78**: 3093.

Bibliography

Ancilotto, F. and F. Toigo, (1994). Phys Rev B **50**(17): 12820-12830.

Atkins, K. R., (1959). The Physical Review **116**(6): 1339.

Barr, J. D., J. M. Dyke, et al., (1998). Journal of Electron Spectroscopy **97**: 159-170.

Biernacki, D. T., S. D. Colson, et al., (1988). J Chem Phys **89**(5): 2599-2608.

Borghesani, A. F. and M. Santini, (2002). Phys Rev E **65**(5): -.

Buzzacchi, M., D. E. Galli, et al., (2001). Phys Rev B **6409**(9): -.

Callicoatt, B. E., K. Forde, et al., (1998). J Chem Phys **109**(23): 10195-10200.

Callicoatt, B. E., K. Forde, et al., (1998). J Chem Phys **108**(22): 9371-9382.

Callicoatt, B. E., D. D. Mar, et al., (1996). J Chem Phys **105**(17): 7872-7875.

Chergui, M., R. Schriever, et al., (1988). J Chem Phys **89**(12): 7083-7093.

Chergui, M. and N. Schwentner, (1989). J Chem Phys **91**(10): 5993-6005.

Chergui, M. and N. Schwentner, (1992). J Chem Phys **97**(5): 2881-2890.

Chergui, M., N. Schwentner, et al., (1986). J Chem Phys **85**(5): 2472-2482.

Cole, M. W. and R. A. Bachman, (1977). Phys Rev B **15**(3): 1388-1394.

Curtis, S., A. Boatwright, et al., (2005). Chem Phys Lett **401**(1-3): 254-258.

Diederich, T., J. Tiggesbaumker, et al., (2002). J Chem Phys **116**(8): 3263-3269.

Doppner, T., T. Diederich, et al., (2001). Eur Phys J D **16**(1-3): 13-16.

Doppner, T., S. Teuber, et al., (2003). Eur Phys J D **24**(1-3): 157-160.

Ellis, T., P. V. E. Mcclintock, et al., (1983). J Phys C Solid State **16**(15): L485-L489.

Emery, L. and K. S. Song, (1986). J Phys C Solid State **19**(14): 2469-2473.

Farnik, M., B. Samelin, et al., (1999). J Chem Phys **110**(18): 9195-9201.

Farnik, M. and J. P. Toennies, (2003). J Chem Phys **118**(9): 4176-4182.

Farnik, M. and J. P. Toennies, (2005). J Chem Phys **122**: 014307.

Foerste, M., H. Guenther, et al., (1998). J Low Temp Phys **110**(1-2): 231-236.

Glaberson, W. I. and W. W. Johnson, (1975). J Low Temp Phys **20**(3-4): 313-338.

Goodman, J. and L. E. Brus, (1977). J Chem Phys **67**(3): 933-940.

Grimes, C. C. and G. Adams, (1990). Phys Rev B **41**(10): 6366-6372.

Gross, M. and F. Spiegelmann, (1998). Eur Phys J D **4**(2): 219-224.

Gspann, J. and H. Vollmar, (1981). J Low Temp Phys **45**(3-4): 343-355.

Halberstadt, N. and K. C. Janda, (1998). Chem Phys Lett **282**(5-6): 409-412.

Henne, U. and J. P. Toennies, (1998). J Chem Phys **108**(22): 9327-9338.

Jiang, T., C. Kim, et al., (1993). Physical Review Letters **71**(5): 700-703.

Jost, R., J. Nygard, et al., (1997). Phys. Rev. Lett **78**: 3093-3096.

Klos, J., G. Chalasinski, et al., (2000). J Chem Phys **112**(5): 2195-2203.

Lee, E. P. F., P. Soldan, et al., (1998). J Phys Chem A **102**(34): 6858-6864.

Lee, E. P. F. and T. G. Wright, (1998). J Chem Phys **109**(1): 157-161.

Lerner, P. B. and I. M. Sokolov, (1989). Z Phys D Atom Mol Cl **14**(2): 173-177.

Levine, J. L. and T. M. Sanders, (1967). Physical Review **154**(1): 138.

Miller, J. C. and R. N. Compton, (1986). J Chem Phys **84**(2): 675-683.

Nakayama, A. and K. Yamashita, (2000). J Chem Phys **112**(24): 10966-10975.

NIST (2005). http://webbook.nist.gov/.

Northby, J. A., C. Kim, et al., (1994). Physica B **197**(1-4): 426-434.

Northby, J. A. and T. M. Sanders, (1967). Physical Review Letters **18**: 1184.

Northby, J. A., S. Yurgenson, et al., (1995). J Low Temp Phys **101**(3-4): 427-432.

Omalley, T. F. and R. W. Crompton, (1980). J Phys B-at Mol Opt **13**(17): 3451-3464.

Ossicini, S., (1985). J Phys Chem Solids **46**(1): 123-126.

Ostermeier, R. M., (1973). Physical Review A **8**: 514.

Ovchinnikov, M., B. L. Grigorenko, et al., (1998). J Chem Phys **108**(22): 9351-9361.

Peterka, D. S., A. Lindinger, et al., (2003). Physical Review Letters **91**(4): -.

Peterka, D. S. and D. M. Neumark (2005).

Polischuk, A. Y., (1983). J Phys B-at Mol Opt **16**(20): 3853-3858.

PortellaOberli, M. T., C. Jeannin, et al., (1996). Chem Phys Lett **259**(5-6): 475-481.

Radcliffe, P., A. Przystawik, et al., (2004). Physical Review Letters **92**(17): -.

Resca, L. and R. Resta, (1979). Phys Rev B **19**(4): 1683-1688.

Robbe, J. M., M. Bencheikh, et al., (1993). Chem Phys Lett **210**(1-3): 170-174.

Roncin, J. Y., H. Damany, et al., (1967). Rev Sci Instrum **22**: 154.

Rosenblit, M. and J. Jortner, (1995). Physical Review Letters **75**(22): 4079-4082.

Ruchti, T., B. E. Callicoatt, et al., (2000). Phys Chem Chem Phys **2**(18): 4075-4080.

Ruchti, T., K. Forde, et al., (1998). J Chem Phys **109**(24): 10679-10687.

Schappe, R. S., R. J. Edgell, et al., (2002). Physical Review A **65**(4): -.

Schoepe, W. and C. Probst, (1970). Phys. Lett. A **34**: 490.

Schwentner, N., E. E. Koch, et al. (1985). Springer.

Shafizadeh, N., P. Brechignac, et al., (1998). J Chem Phys **108**(22): 9313-9326.

Shikin, V. B., (1977). Usp Fiz Nauk+ **121**(3): 457-497.

Soldan, P., E. P. F. Lee, et al., (2002). J Chem Phys **116**(6): 2395-2399.

Springett, B. E., (1967). Physical Review **155**: 139.

Stienkemeier, F. and A. F. Vilesov, (2001). J Chem Phys **115**(22): 10119-10137.

Stolyarov, D., E. Polyakova, et al., (2004). J Phys Chem A **108**(45): 9841-9846.

Toennies, J. P.

Toennies, J. P. and A. F. Vilesov, (2004). Angew Chem Int Edit **43**(20): 2622-2648.

Vigliotti, F., L. Bonacina, et al., (2003). Phys Rev B **67**(11): -.

Vigliotti, F., A. Cavina, et al., (2002). J Chem Phys **116**(11): 4542-4552.

Vigliotti, F. and M. Chergui, (1998). Chem Phys Lett **296**(3-4): 316-322.

Vigliotti, F., M. Chergui, et al., (1997). Faraday Discuss(108): 139-159.

von Haeften, K., A. R. B. de Castro, et al., (1997). Physical Review Letters **78**(23): 4371-4374.

von Haeften, K., T. Laarmann, et al., (2005). J Phys B-at Mol Opt **38**(2): S373-S386.

Wade, E. A., J. I. Cline, et al., (2002). J Chem Phys **116**(12): 4755-4757.

Zacharias, H., F. deRougemont, et al., (1996). J Chem Phys **105**(1): 111-117.

Zacharias, H., J. B. Halpern, et al., (1976). Chem Phys Lett **43**(1): 41-44.

Zerza, G., F. Vigliotti, et al., (1996). Chem Phys Lett **256**(1-2): 63-70.

Zolotoukhina, T. N. and S. Kotake, (1993). J Chem Phys **99**(4): 2855-2864.

Appendixes

Appendix A. Alignment of a helium droplet machine with a telescope

Assembly or modification of a helium droplet machine or any molecular beam apparatus requires the precise alignment of all internal apertures and skimmers. Even a slight misalignment causes partial destruction of the helium droplet beam and back-scattering of helium gas, which causes further destruction of the helium droplet beam. That is why the deviation in alignment of the internal apertures should not exceed 1 mm. This precision cannot be achieved with a He-Ne laser because of diffraction of the laser beam on apertures.

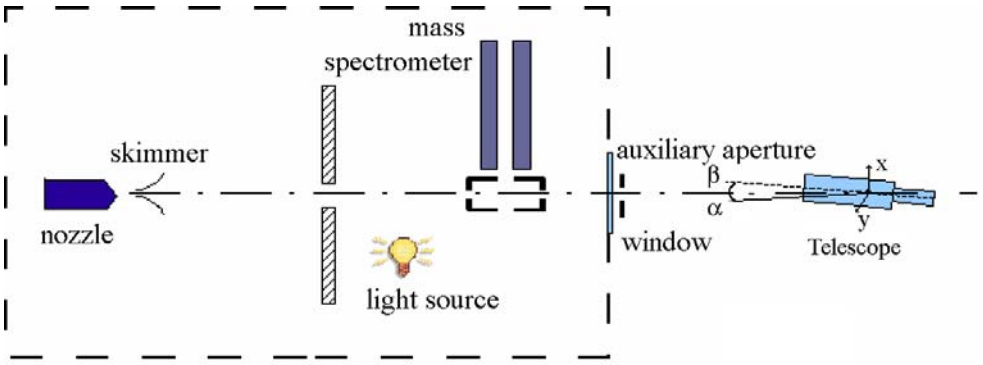

Figure A-1. Alignment scheme. x – horizontal, y – vertical positions of the telescope, α- wag, ß - tilt angles.

In contrast, a telescope is a very helpful tool. Since industry does not produce any special equipment for helium machine alignment, an industrial optical surveying level (Nikon AE-7) is used. A high magnification ratio allows

more precise alignment of machine, but if the machine is severely misaligned, it may be difficult to determine how to align it because only a small magnified spot at the chamber wall is visible. In addition, luminosity drops with magnification, so an additional light source might be needed inside the chamber. The telescope used has ×30 magnification, which is not the largest magnification available, but it fits the needs of experiment perfectly. The most convenient feature is a low minimum focusing distance. The first alignment aperture should be reachable by hand, so the minimum focusing distance should be less than 0.5 m. In this case, it is 0.3 m.

While aligning the telescope along the helium machine axis, the horizontal and vertical position, and the tilt and the wag angles of the telescope should be controllable. Once the telescope is aligned, its position must be fixed. For this reason, a stopper screw was added to modify the telescope. One more a telescope feature is an automatic level compensator, which aligns the telescope horizontally, therefore, improving its functionality as a level. However, the axis of the chamber can be not horizontal. If one decides to use one of the alignment schemes described below, this feature is useless. The axis of the machine is defined by two reference points located at both ends of the chamber. It is convenient to choose skimmer orifice and the center of the ionization region of the quadrupole mass spectrometer as the reference points. The nozzle orifice is difficult to see behind the skimmer. In addition, it is a bad idea to use it as a reference point because the nozzle moves as the droplet machine cools down. Once the axis of the chamber is

defined, the axis of the telescope must be aligned along the axis of the chamber. To do that, the vertical and horizontal positions (x and y, Fig. A-1) and the wag and tilt angles (α and ß) must be adjusted. The problem is to find a reliable mount with fine adjustment controls for the telescope. The adjustments of a surveying level, as it comes from the manufacturer, may be not good enough. For example, there can be no wag angle adjustment or no stopper, or, the adjustments may be not fine enough.

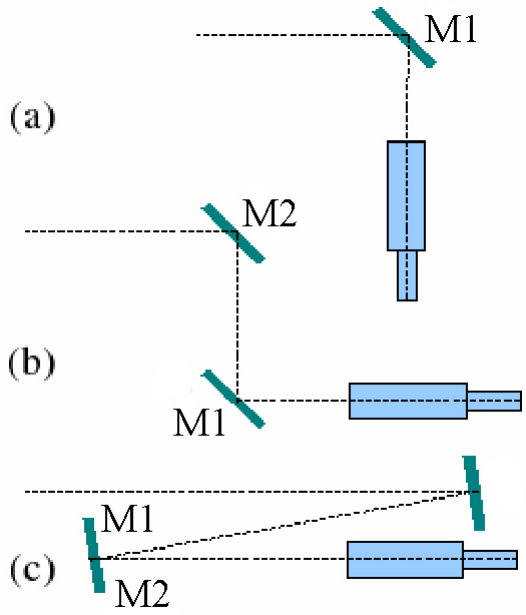

Figure A-2. Alignment schemes.

To avoid this problem, one or two mirrors (Fig. A-2) can be used. It is easier to a find high-quality mount for a mirror than for the telescope. A 4' protected Al mirror (protected Ag is good as well) mounted on Ultima U400-AC (Newport Corp) was used. The alignment assembly is shown in Fig. A-2 (a). On

the other hand, the schemes with 2 mirrors, Fig A-2 (b) and (c), may be more reliable. If one of these schemes is decided upon, the telescope position should be fixed, and the telescope adjustments must be used for rough alignment. Then, fix these adjustments with a drop of epoxy glue on the adjustment threads.

The alignment is an iterative procedure. First, the telescope should be focused on the skimmer orifice and its position should be centered on the telescope steering mirror M2. Then, the telescope should be focused at the center of the mass spectrometer ionization and it should be centered on the telescope steering mirror M1. These two steps must be repeated until both the skimmer orifice and the ionization region of the mass spectrometer are centered. If one mirror is used (Fig A-2 (b)), the procedure depends upon the adjustments of the telescope. If the angles of the telescope should be adjusted, the skimmer orifice and center ionization region of the mass spectrometer should be centered by steering the mirror. The alignment procedure must converge. If iterations move the system away from alignment, the order of the iterations must be changed. Once satisfied with the alignment, the adjustment screws should be fixed. As the next step, an iris diaphragm must be installed in front of the chamber with the help of the telescope.

Appendix B. Nozzle check-up procedure

After the installation of the copper disk with 5μm aperture (Fig. 3-4, part 2), it is important to check the nozzle before the cryogenic helium droplet source

is assembled. There are three common problems. First, the aperture completely or partially clogged during fabrication. It is always a good idea to order at least five disks. (The price of one disk is $84, National Aperture) Second, the indium gasket (Fig. 3-4, part 4) can be damaged during the disk installation. Third, if the gasket is not installed property, helium leaks between the gasket and the nozzle (Fig. 3-4, part 3). This simple check-up procedure, which takes less than 20 minutes, can save several days of work if the problem is found only when the droplet source is pumped out and cooled down.

The check-up procedure is as follows: connect the helium line with pressure 20 bar to the assembled nozzle. For this purpose it may be convenient to have a flexible tube attached to the same helium line that is used for helium droplet production. Check the Swagelok connections with a leak detector (Snoopy©). Then, put the nozzle inside a large beaker with alcohol. Bubbles coming from the aperture must be visible. If not so, the nozzle is clogged, and the copper disk must be replaced. Ensure that all helium flux goes through the aperture. To check that there is no leak between the gasket and the nozzle, it is convenient to drill a small hole in a nut (Fig. 3-4, part 3). If there is a leak, the bubbles from this hole would be seen. Even the tiniest bubbling cannot be ignored; when the nozzle is cooled down to cryogenic temperatures, the leak increases dramatically. The next step is to measure the flux of the helium. If the nozzle is good, the flux must be 20 ml per 30 seconds, and the volume of gas can be measured by graduated cylinder. If the flux is good, remove the nozzle from

the beaker and leave it under pressure for one minute before disconnecting the helium line.

Appendix C. The procedure of the nozzle alignment

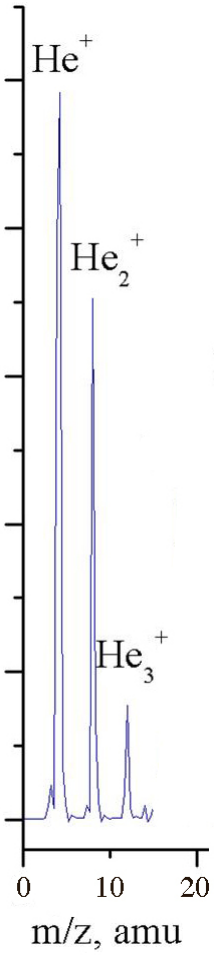

Figure A-3 Example of mass spectrum for well-aligned nozzle

The purpose of nozzle alignment is to maximize the flux of the helium droplets through the ionization region of the mass spectrometer. In particular, the ion signal of helium dimer He_2^+ is to be optimized. The nozzle position can be adjusted by two linear motion manipulators (see Chapter 3) with an accuracy of 0.001 in. The maximum displacement of the nozzle aperture is ± 10 mm in X direction and ± 5mm in Y direction. The coordinate Z (distance from nozzle to skimmer) is fixed during the experiment, but can be changed manually by ± 5mm.

While the nozzle is cooling, the flux of helium grows with time

and the entire cryogenic source contracts; therefore, the position of the aperture must be aligned with respect to the skimmer only after the cryogenic nozzle reaches working temperature (T < 20K). If the nozzle aperture is far from the optimal position, only a He^+ signal is visible on the mass spectrum. The complete absence of a He^+ signal is a sign that the nozzle is clogged and is to be replaced. First, the signal from helium monomer He^+ should be maximized. This signal should be at least an order of magnitude higher than the signal from background gases (water, hydrogen, pump oil vapors).As soon as the direct droplet beam attains the mass spectrometer, the dimer signal must appear. Once a He_2^+ signal is visible, it must be maximized. An example of the mass spectrum of pure helium droplet beam, if the cryogenic nozzle operates and is properly aligned, is shown in Fig. A-3 (T = 15 K, p = 40 bar). One should note that

$$\frac{I\left(He_2^+\right)}{I\left(He_3^+\right)} \approx 6$$

If this ratio is higher than 10 for similar experimental conditions, the droplet beam could be partially destroyed due to poor alignment of the experimental apparatus (Appendix B).

Appendix D. The laser beam alignment procedure

Since even a minor misalignment of the laser beam causes severe changes, it is extremely important to develop a procedure to ensure that the laser beam is returned to the same position everyday. Initially, an approximate position of the

intersection of the laser and helium beams can be found by visual alignment. At first, helium beam trajectory can be simulated by helium-neon laser that is guided by previously installed iris (see Appendix A). The ionization laser must be propagated through the geometrical center of the entrance and exit windows. In our chamber one of the walls can be removed, and an object that scatters light (bead, cotton ball, etc.) can be placed at the cross point of these two lasers, and the intersection point of the two laser beams can be found. (See Fig. A-4)

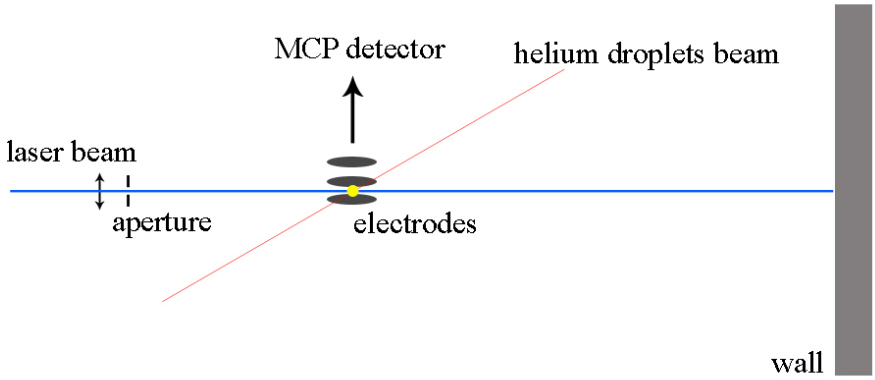

Figure A-4. Laser beam alignment scheme.

After the vacuum chamber is pumped out and the ionization signal is visible, the exact position that corresponds to the maximum of the signal can be found. (It is almost impossible to find it without the preliminary alignment). Once found, the position of the ionization laser is fixed by two reference points. The iris in the front of the chamber was used as the first reference point and a mark one a wall as the second reference point. The spatial position of laser beam can fluctuate during the day and must be checked every several hours.